University of California, Davis

RADIOLOGY RESEARCH SYMPOSIUM

September 18, 2023

Program and Abstracts

UC DAVIS HEALTH | Department of Radiology

2023 Radiology Research Symposium Program and Abstract Table of Contents

CHAIR'S MESSAGE AND WELCOME

We are very excited to showcase and share some of the exciting work underway in the realm of medical imaging and clinical research as part of our 2nd Annual Radiology Research Symposium. This day will highlight advances in imaging research by featuring work from our faculty, fellows, residents, medical students, graduate trainees, and even local high school students.

The UC Davis Department of Radiology has a track record of exciting innovations, pursuing discovery and health care advances across multiple radiology specialties. This symposium will be an opportunity for attendees to see both the new and exciting directions our field is moving and gain insight into the latest technologies and innovations underway here at UC Davis that will impact patient care of the future. We have a total of 44 posters on display and some exciting talks to be presented throughout the day that will prove to be both interesting and informative.

Radiology converges with virtually all specialties in healthcare and what we do allows others throughout the medical profession to deliver the best care possible to our patients. The novel medical imaging technology and techniques being studied today translate into the innovations of tomorrow that will allow us to visualize and diagnose diseases earlier and earlier, and to track the success of treatments with a precision never before possible.

We are excited to share with you what we are doing currently and how we see the future of healthcare!

Elizabeth A. Morris, M.D.

Chair, Department of Radiology

2023 Radiology Research Symposium Program

The Future of Clinical Research at UC Davis Radiology

3 p.m. Chair's Introduction - Elizabeth Morris, M.D.

3:05 p.m. VC Research Introduction - Ramsey Badawi, Ph.D.

3:10 p.m. Session 1: Vision Talks – 15 minutes each, 5 minutes discussion

- **Moderators – Michael Corwin, M.D. and Shadi Aminololama-Shakeri, M.D.**

Emerging AI Applications for Breast Imaging	Elizabeth Morris, M.D.
Research Opportunities in Abdominal Imaging	Ramit Lamba, M.D.
Neuroimaging Research Opportunities at UC Davis	Kader Karli Oguz, M.D.

4:10 p.m. Break

4:25 p.m. Session 2: Vision Talks – 15 minutes each, 5 minutes discussion

- **Moderators – Abhijit Chaudhari, Ph.D. and Tony Seibert, Ph.D.**

Toward a Greener Tomorrow: Collaborative Efforts to Reduce Healthcare's Carbon Footprint	Andrew Hernandez, Ph.D.
Large Language Models in Radiology – Current and Future Uses	Thomas Loehfelm, M.D., Ph.D.

5:05 p.m. Selected Abstract Presentations

First-in-Human Study of the Theranostic Pair [68Ga]Ga DOTA-5G and [177Lu]Lu DOTA-ABM-5G in Pancreatic Adenocarcinoma	Cameron Foster, M.D.
Reconstruction-Free 3D Imaging of Positron-Emitting Radiotracers Using Ultrafast Detectors and Artificial Neural Network	Sun Il Kwon, Ph.D.

5:20 p.m. Abstract Awards – Guobao Wang, Ph.D.

5:30 p.m. Closing Remarks – Michael Corwin, M.D.

5:35 p.m. Posters and Food

7 p.m. Close

Characterizing the Spectrum of Spinal Inflammation in Psoriatic Arthritis by in-vivo ^{18}F-FDG Total-Body PET/CT Imaging: Initial Findings

Yasser G. Abdelhafez, M.D., Ph.D.; Dario F. Mazza, M.Sc.; Smriti K. Raychaudhuri, M.D.; Siba P. Raychaudhuri, M.D.; Abhijit J. Chaudhari, Ph.D.

Introduction: Axial involvement, characterized by inflammation and post-inflammatory structural changes of the spine and/or sacroiliac joints, may occur in 25-70% of patients with psoriatic arthritis (PsA). However, imaging characterization of spinal inflammation is quite challenging. We aimed to describe the spectrum of spondylitic changes demonstrated on Total-Body (TB) PET/CT imaging using ^{18}F-FDG in patients with PsA.

Methods: Twenty-four PsA participants; 8 patients with inflammatory back pain.

- 18F-FDG PET using 1/5th the standard dose.
- Ultra-low-dose CT (~1 mSV).
- Qualitative and quantitative features were evaluated for atlantoaxial, apophyseal, costovertebral/costotransverse, and sacroiliac joints involvement. Entheses (cervical/thoracic/lumbar supra- and interspinous ligaments) were also evaluated.

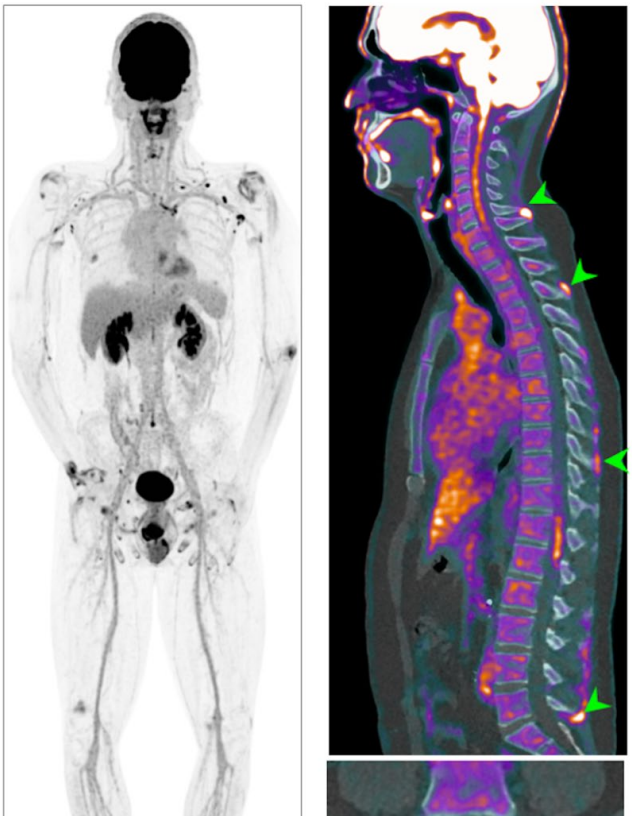

Supra-/inter-spinous enthesitis. TB-PET/CT in a 33-year-old man with PsA. The total-body PET maximum intensity projection image (left) shows numerous joint abnormalities. Multiple active spinal entheses are seen in cervical, thoracic, and lumbar spine (right top image, arrowheads), albeit with no evidence of sacroiliac joint involvement (right bottom image).

Results:

- Qualitatively, TB-PET demonstrated abnormality in ≥1 evaluated site(s) in 21 (88%) patients, including all 8 pts. with inflammatory back pain:
  - 83% showed spinal enthesitis on PET including two patients with no structural evidence of arthritis or sacroiliitis.
  - 63% showed atlantoaxial and 78% showed apophyseal involvement.
  - A few patients demonstrated evidence of sacroiliitis on PET (n=4). The involvement was unilateral in 2 patients and bilateral but asymmetric in the other 2 patients.
- Quantitatively, the summed relative SUVmax for all the described sites was 7.3±3.1 per patient.

DISCUSSION: Spondylitic changes were prevalent among patients with PsA with more than 80% demonstrating involvement of the entheses at the posterior vertebral elements; this could be the primary pathology for axial inflammation in PsA. In majority of the patients, axial involvement was clinically occult, as only about one third of the patients reported back pain, which raise the potential for identification of non-radiographic axial spondyloarthritis.

Conclusion: ^{18}F-FDG TB-PET/CT may enable characterization of the axial inflammation, an important disease domain in the otherwise highly heterogeneous PsA disease pathology. Future studies will focus on extending evaluation to other sites and features (e.g., new bone formation), studying effects of different treatment approaches, and comparing to another imaging modality.

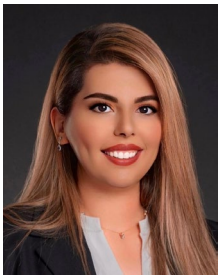

Role of MRI in pediatric cervical spine clearance after trauma and negative cervical spine CT

Nazanin Azizi, M.D., Jimmy L. Huynh, M.D., Ph.D., Matthew Bobinski, M.D., Ph.D., Osama Raslan, M.D., Lotfi Hacein-Bey, M.D., and Arzu Ozturk, M.D.

Introduction: The cervical spine in children has marked anatomical and biomechanical differences compared to adults, leading to significantly different patterns, mechanisms and incidence of spine injury, [1] and consequently to differences in X-Ray and CT imaging recommendations. [2] Cervical spine MRI has been validated to clear cervical spine trauma in adults, but not in pediatric patients. [3] We hypothesized that MRI findings have a low probability to change management in children with spine trauma and negative CTs.

Methods: Retrospective review of children (age ≤ 18) with neck trauma who received a CT of the cervical spine followed by MRI within 3 days of CT (n=255) by two neuroradiologists (JLH, AO). Systematic review of CT and MRI for: fracture, subluxation, spinal canal compromise, ligamentous injury, spinal canal hemorrhage, or soft tissue hemorrhage. Negative C-spine CT studies were first selected. In that cohort, follow up MRI was then categorized as negative or positive.

Results: Out of 255 patients, 212 had a negative CT. The majority (79.7%) had no detectable abnormality on follow up MRI. The primary positive MRI finding was ligamentous sprain without disruption (14.2%). In a minority of cases (6.1%) a finding requiring additional follow up, i.e. cord contusion, epidural hematoma, or focal ligamentum flavum disruption was present. Focal ligamentum flavum disruption was the only injury associated with completely negative CT findings. In the remainder, remote secondary findings such as posterior fossa, skull base or thoracic spine injury were found.

Conclusion: In our study of children with cervical spine trauma and a negative CT, the majority of follow-up MRI scans were negative, therefore with no role in cervical spine clearance. Positive MRI findings were mainly ligamentous sprain. Exceptionally, MRI may demonstrate cervical cord findings in patients with traumatic injury at the skull base or thoracic spine. [4]

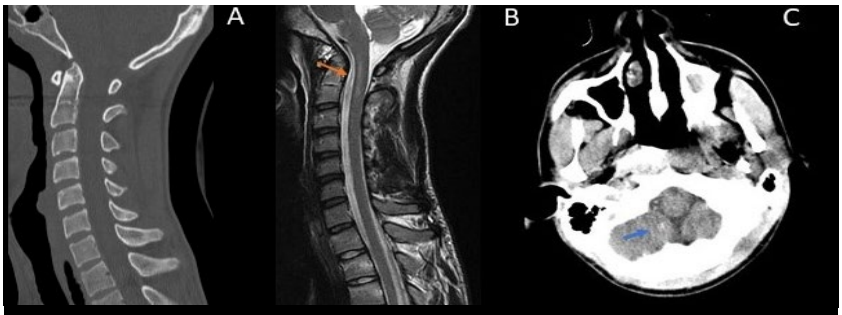

Figure. Upper cervical cord contusion as a secondary finding. (A) C-Spine CT shows no abnormalities, (B) MRI shows focal area of T2 hyperintensity at C1-2 (orange arrow), (C) CT, wide window shows hemorrhagic contusion in the right cerebellar tonsil (blue arrow).

References

1. Carreon LY, Glassman SD, Campbell MJ. Pediatric spine fractures: a review of 137 hospital admissions. *J Spinal Disord Tech*. 2004;17(6):477-482.
2. McAllister AS, Nagaraj U, Radhakrishnan R. Emergent Imaging of Pediatric Cervical Spine Trauma. *Radiographics*. 2019;39(4):1126-1142.
3. Wang MX, Beckmann NM. Imaging of pediatric cervical spine trauma. *Emerg Radiol*. 2021;28(1):127-141.
4. Hacein-Bey L. SCIWORA no more? The case for targeted cervical spine MRI in blunt trauma. J Neuroradiol. 2021 May;48(3):139-140. doi: 10.1016/j.neurad.2021.04.034. PMID: 33958135.

Laser Interstitial Thermal Therapy (LITT)-Related MRI Findings in Pediatric Posterior Fossa Brain Tumors

Nazanin Azizi, Arzu Ozturk, Yasamin Mohammad, Osama Raslan, Reuben Antony, Marike Zwienenberg, Orin Bloch, Michael Edwards, Kader Karli Oguz

Introduction: Laser interstitial thermal therapy (LITT) has been increasingly used in the management of brain lesions as a less-invasive treatment compared to conventional surgery (1). Reports to date are limited on LITT application of pediatric posterior fossa tumors (2). We present LITT related evolutionary MRI changes in three pediatric patients with posterior fossa tumors to increase awareness among radiologists.

Materials and Methods: We retrospectively documented 3 pediatric patients who received LITT treatment for recurrent/residual posterior fossa tumors including WNT-activated medulloblastoma, ependymoma, PFA-molecular subgroup; Rosette Forming Glioneuronal Tumor. Post LITT MRIs were obtained at procedure day and follow-ups at 1, 2, and 4 months.

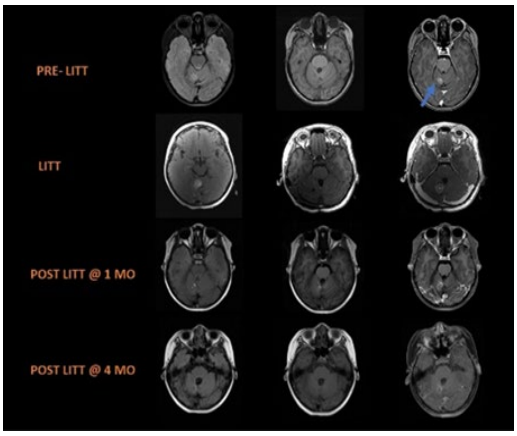

Results: Treatment related changes reflected central and peripheral zones of the laser needle probe, peripheral zone and perifocal edema. Early post procedure MRI demonstrated rim of diffusion restriction at the margin of the treatment zone followed by a ring of contrast enhancement with/without target appearance, perilesional edema, and increase in size of lesion in all cases similar to previous reports in the literature (3). There were follow-up MRIs at 1 and 4 months of the patient with medulloblastoma (Figure) and RGNT cases and only at 1 month in the patient with ependymoma. All showed gradual resolution of surrounding edema, evolution of hemorrhagic changes into subacute phase, decreased enhancement. Reduced size of the targeted tumors was observed. However, patient with RGN patient showed progression at 4mos follow-up.

Conclusion: LITT has been increasingly used and has proved to be an effective tool for inaccessible or recurrent tumors and for patients who will not tolerate open surgery. Multilayered rings of enhancement, evolving blood products and edema are the most typical MRI abnormalities in these patients. Awareness of the post LITT evolutionary MRI patterns will enable radiologists to interpret MRI changes accurately.

References:
1. Kuo CH, Feroze AH, Poliachik SL, Hauptman JS, Novotny EJ Jr, Ojemann JG. Laser ablation therapy for pediatric patients with intracranial lesions in eloquent areas. World Neurosurg. 2019;121:e191–e199.
2. Tovar-Spinoza Z, Choi H. Magnetic resonance guided laser interstitial thermal therapy: report of a series of pediatric brain tumors. J Neurosur Pediatr. 2016;17:723-733.
3. Hawasli AH, Bagade S, Shimony JS, Miller-Thomas M, Leuthardt EC: Magnetic resonance imaging-guided focused laser interstitial thermal therapy for intracranial lesions: single institution series. Neurosurgery 73:1007–1017, 2013

An In-House Image Reconstruction Framework with Accelerated, Serverless Scatter Correction for Total-Body PET

R. Bayerlein[1], Vivek Swarnakar[2], B. A. Spencer[1,3], A. Selfridge[1], Q. Wang[3], L. Nardo[1], S. R. Cherry[3,1], R. D. Badawi[1,3]

[1]*Department of Radiology, UC Davis Health, Sacramento, CA, USA*
[2]*Imaging consultant, UC Davis*
[3]*Department of Biomedical Engineering, University of California Davis, CA, USA*

Modern positron emission tomography (PET) requires complex image reconstruction and data correction algorithms to create images of high diagnostic quality. In recent years, we have been developing, improving, and validating a UC Davis in-house framework with a graphical user interface for the reconstruction of total-body PET data acquired with the uEXPLORER.

One focus point in the development was the implementation of scatter correction (SC) using Monte Carlo (MC) methods. Despite proven reliability and accuracy, MC methods present considerable computational challenges for SC in total-body PET, due to the extensive number of lines of response and increased acceptance angle. Thus, the computation of the required simulation data using multi-core CPUs on our local server took several hours – rendering this approach impractical for routine clinical PET image reconstruction.

To improve computation time by an order of magnitude, we implemented an accelerated cloud-based serverless infrastructure using Amazon Web Services (AWS) Lambda. The utilized MC tool SimSET is well-suited for such large-scale distributed parallel computing. Upon completion the resulting list-mode files of simulated true and scattered event from all instances are merged and downloaded for further SC processing. The implemented architecture is depicted in Figure 1.

For performance evaluation, we conducted simulations with varying numbers of simulated decays, ranging from 10^5 to $2{\cdot}10^{10}$, distributing the total number of decays across 1000 AWS Lambda instances and the on-premises server, respectively.

Our findings indicate that leveraging cloud-based serverless computing resources can lead to considerable performance improvements: in our research image reconstruction pipeline with 10^{10} simulated events per iteration an improvement by a factor of 10.1 was obtained. However, internet connection speeds remain as the primary bottleneck for this implementation.

In this contribution we will present some features and capabilities of the in-house image reconstruction framework as well as the accelerated SC algorithm.

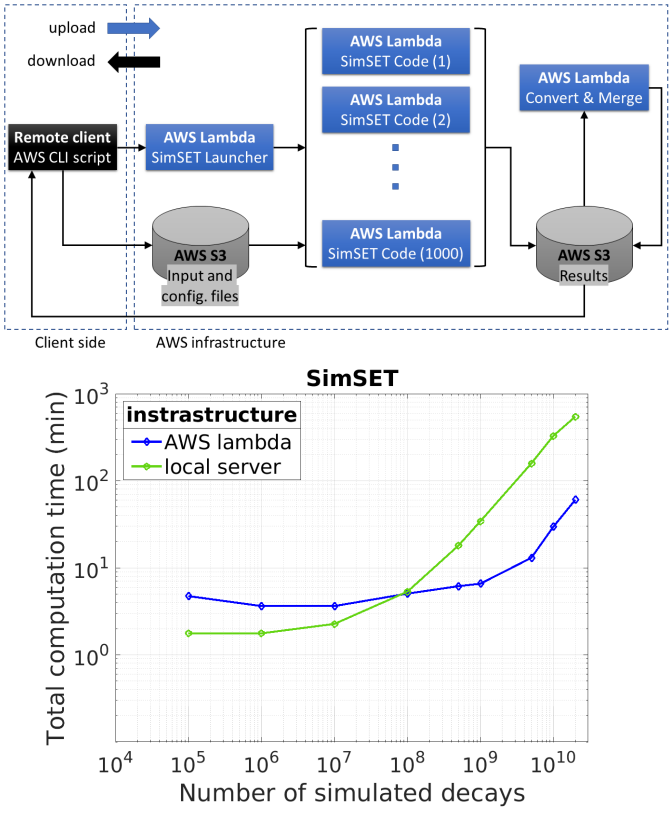

Fig. 1. Top: Interface between a remote client, a cloud storage service (AWS S3) and computing units (AWS lambda) executing parallel SimSET simulations for SC. Bottom: at large event numbers, AWS performs over one order of magnitude faster than our on-premises reconstruction server.

A guidewire trajectory simulation tool for MRI electric fields

Fatima Ben Haj[1], Felipe Godinez[2]

[1]Davis Senior High School, California, Davis, USA
[2]Department of Radiology, University of California Davis, Sacramento, California, USA

Introduction: Interaction of guidewires with MRI RF coils has been studied experimentally, however in practice guidewire trajectories can vary greatly, and this effect is hard to capture with experiments. The goal of this work is to develop a simulation approach to generating a significant number of trajectories that capture this effect.

Methods: We created a function using MATLAB to simulate guidewire trajectories through an electric field in a digital human phantom. A graphical user interface allows the user to manually pick points and ranges, which are connected using the spline function cscvn(). Each trajectory is created by generating random points within the ranges. Trajectories are modified to a desired length by removing points from the proximal end of the guidewire. The user can also define the number of random points they want generated within the range for each point, in a variable called ‘step’. A higher ‘step’ means more trajectories are generated. The spline is then displayed over the user’s inputted electric field. The function was run on a personal laptop computer.

Results: The program outputs a list of spatial coordinates for each generated trajectory (figure 1a). Figure 1b demonstrates an overlay of the trajectories over a user defined electric field. An optional output is a histogram displaying the unmodified and modified guidewire length and a 3D plot of the guidewire, which is useful for visualizing the desired trajectory.

Discussion:
A key feature of the function is to maintain a nominal length. Modifying the length by removing spline points from the proximal end has its limitation because the distance between points on the spline are not constant. Inaccuracy can be up to one centimeter.

Conclusion: We have developed a function that can generate thousands of trajectories that are useful in simulations where calculating the effects of incident RF electric fields on implanted wires is needed.

A

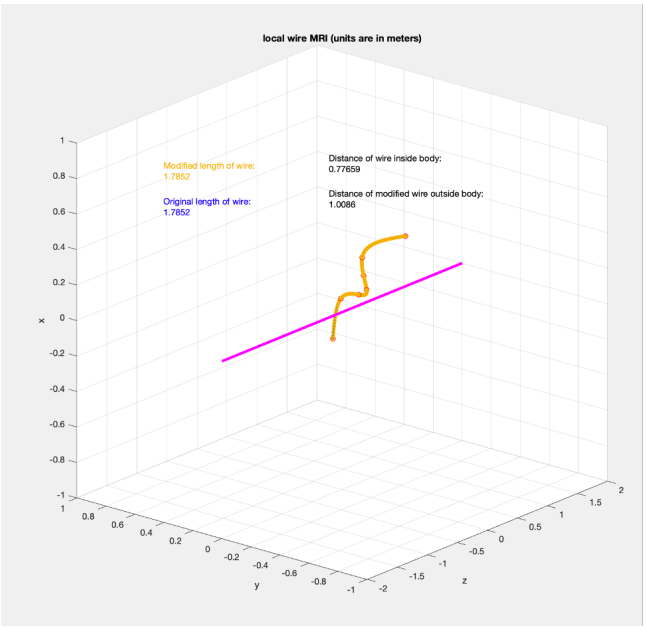

B

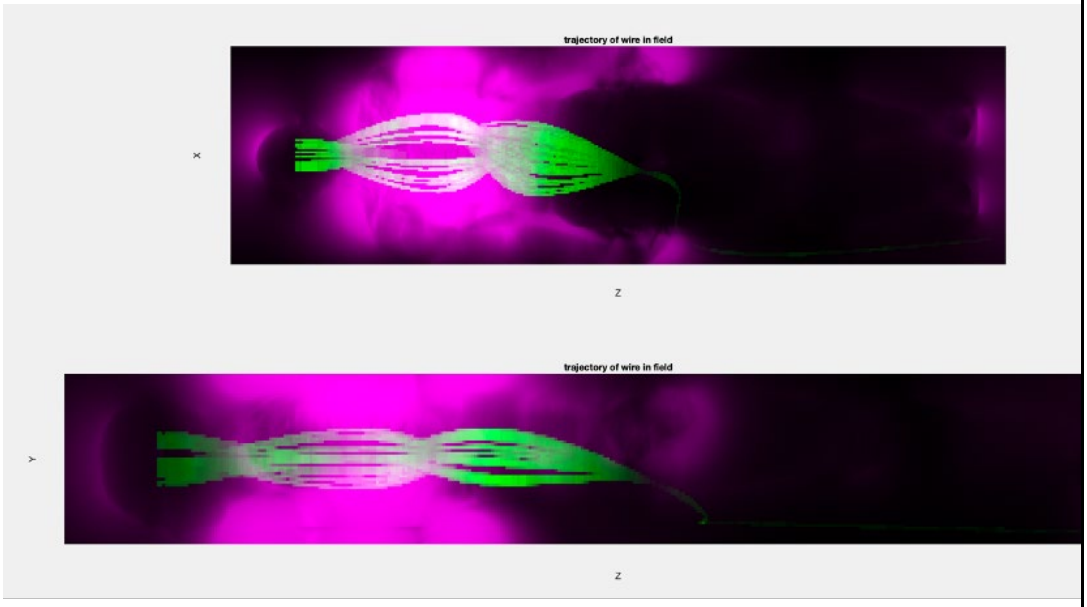

Fig. 1. (A) A 3D plot of a single wire trajectory, yellow curve, as output by the function. (B) Shows the generated trajectories in the given ranges. This plot is in the user provided electric field, simulated in a finite element model.

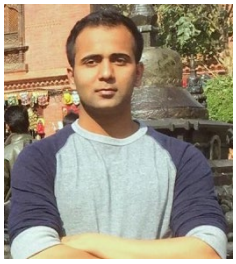

Kinetic modeling of [^{18}F]-PI-2620 binding to tau deposits in the brain using an image-derived input function

Anjan Bhattarai, Ph.D.[1,2*], Emily Nicole Holy, B.S.[1], Yiran Wang, B.S. [2,3], Benjamin A. Spencer, Ph.D. [3], Guobao Wang, Ph.D. [3], Charles DeCarli, M.D.[1], Audrey P. Fan, Ph.D. [1,2]

[1] Department of Neurology, University of California Davis, Davis, CA, USA
[2] Department of Biomedical Engineering, University of California Davis, Davis, CA, USA
[3] Department of Radiology, University of California Davis, Davis, CA, USA

Introduction: This study utilizes non-invasive Image-Derived Input Functions (IDIFs) derived using a total-body EXPLORER PET/CT scanner, to quantitate tau binding from [^{18}F]-PI-2620 PET in the brain and explore its association with age.

Methods: The study cohort included 8 individuals (7 cognitively unimpaired, 1 MCI) of the UC Davis Alzheimer's Disease Research Center. Dynamic total body [^{18}F]-PI-2620 PET images were acquired (90min) using EXPLORER, and reconstructed (resolution=2.344mm, framing protocol:30×2s, 12×10s, 7×60s, 16×300s). The dynamic brain-cropped images were motion corrected (Jenkinson et al., 2002), and linearly registered to individual subject's T1W image (Jenkinson & Smith, 2001). Grey matter brain regions of interest (ROIs), namely medial temporal (MT), posterior cingulate (PC), and lateral parietal (LP), were obtained using T1-weighted image-based FreeSurfer cortical parcellation (Fischl, 2012). Dynamic TACs for each brain ROIs were fit to the two-tissue compartmental model (2TCM), using a subject-specific IDIF derived from the descending aorta. Kinetic parameters were estimated and correlated with age.

Results: Moderate correlations between tracer arrival delay and age were observed in LP (r = 0.56), MT (r = 0.57), and PC (r=0.52). Furthermore, a negative correlation between BP and age in PC (r = -0.53) was found. Significant negative correlation was observed between perfusion (K_1) and binding potential (BP) in the combined ROI (r= -0.73; p<0.001).

Discussion: The positive correlation between delay and age possibly reflects microvascular elongations with ageing. The strong negative correlation between K_1 and BP is an interesting observation and possibly reflects the saturation effect. i.e., the targeted brain ROI may be already occupied with the tracer, and further increase in K_1 might not lead to a proportional increase in BP. Our current and future research will be investigating these associations in a larger cohort.

Conclusion: This study highlights the utility of IDIF from total-body PET in estimating [^{18}F]-PI-2620 kinetics in the brain grey matter regions

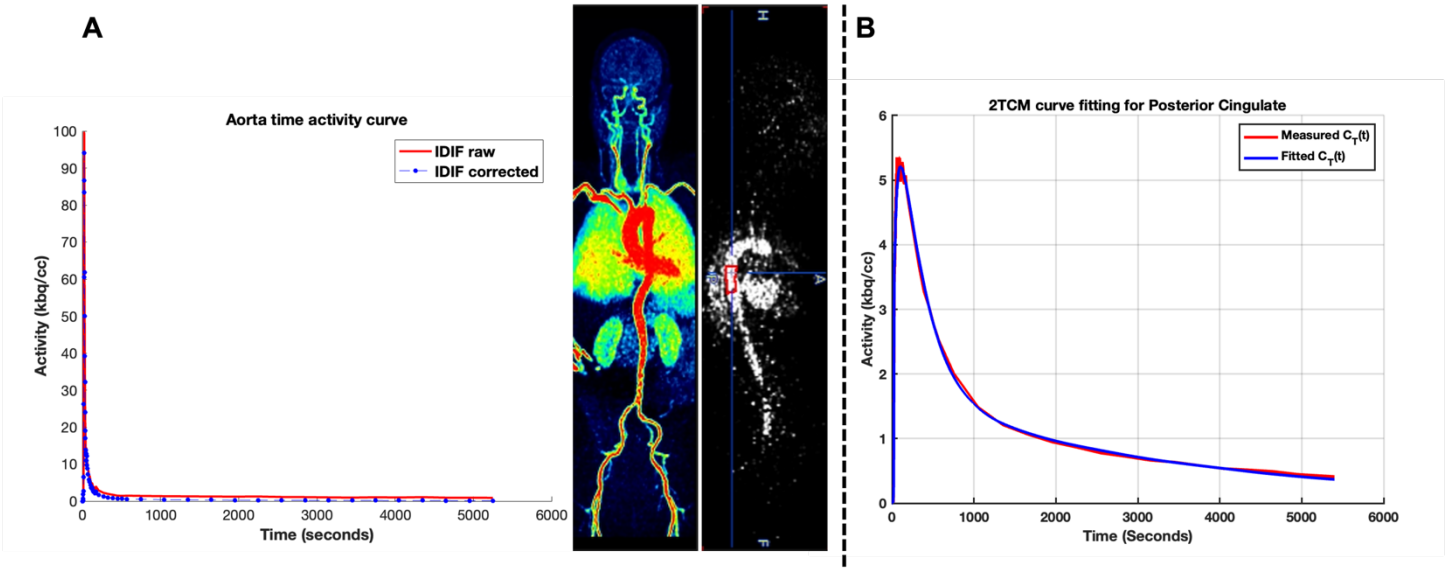

Figure 1: Descending aorta time-activity curve; IDIFs were plasma and metabolite corrected (A). 2TCM curve-fitting demonstration for the posterior cingulate (B).

Impact of Interpretation Speed, Shift Volume, Trainee Participation, Exam Setting on Neuroradiology Errors

Garrick Biddle M.D.[1], Vladimir Ivanovic M.D.[2], Kenneth Broadhead[1], Ryan Beck M.D. [2], Yu-Ming Chang M.D., Ph.D., Alireza Paydar M.D.[1], Lotfi Hacein-Bey M.D.[1], Lihong Qi Ph.D.[1]

UC Davis Medical Center[1]
Medical College of Wisconsin[2]
Beth Israel Deaconess Medical Center[3]

Background: Medical Errors are the third leading cause of mortality in the United States. Median plaintiff and settlement awards for claims involving diagnostic and interventional neuroradiology range between 1.9 and 2.9 million USA dollars.

Objective: Evaluate risk factors for errors by attending neuroradiologists at academic medical center.

Methods: Retrospective study of Quality Assurance (QA) database of consecutive neuroradiology attending diagnostic errors from 2014-2020. CT/MRI exams containing an error formed the Study group. The Control group consisted of interpreted studies not containing an error, matched by radiologist, study type. Conditional and marginal mixed effects logistic regression models were used to study the associations of error status with each of the potential risk factors - study interpretation Time, shift Volume, Emergency setting, Weekend interpretation, Double Read (trainee participation).

Results: The Study group contained 564, and Control 1019 studies, mean age 50.0 +/-25.0 (54.8% men) and 52.5 +/-23.2 years (53.0% men), respectively. Mean interpretation Time was longer, Volume higher in the Study group, 16.3 (+/-17.2) minutes; 50.0 (+/-22.1) studies, compared to 14.8 (+/-16.7); 45.4 (+/-22.9), respectively. Volume was higher on Weekends (76.6 +/- 18.3 and 75.5 +/- 13.7), compared to Weekdays (40.4 +/- 19.4 and 43.5 +/- 18.9) for the Control and Study groups, respectively. Simple mixed effects logistic regression models showed that Volume and Weekend were significantly associated with radiological errors ($p < 0.05$ both models). Weekend was significantly associated with errors (OR > 1.6, $p < 0.001$, both models). Double Read, Emergency setting were not associated with errors ($p > 0.1$, both models). Multiple marginal mixed effects logistic regression model showed Weekend, interpretation Time, Volume significantly associated with radiological errors (aOR=1.69, 95%CI =1.01 - 2.91, p=0.02; aOR=1.18, 95%CI=1.06 - 1.31, p=0.003; aOR=1.27, 95%CI=1.11 - 1.46, p=0.0007). Conditional model yielded similar results for all three risk factors.

Conclusion: Our study showed a significant association between diagnostic errors and weekend shift, high study volume and longer interpretation times.

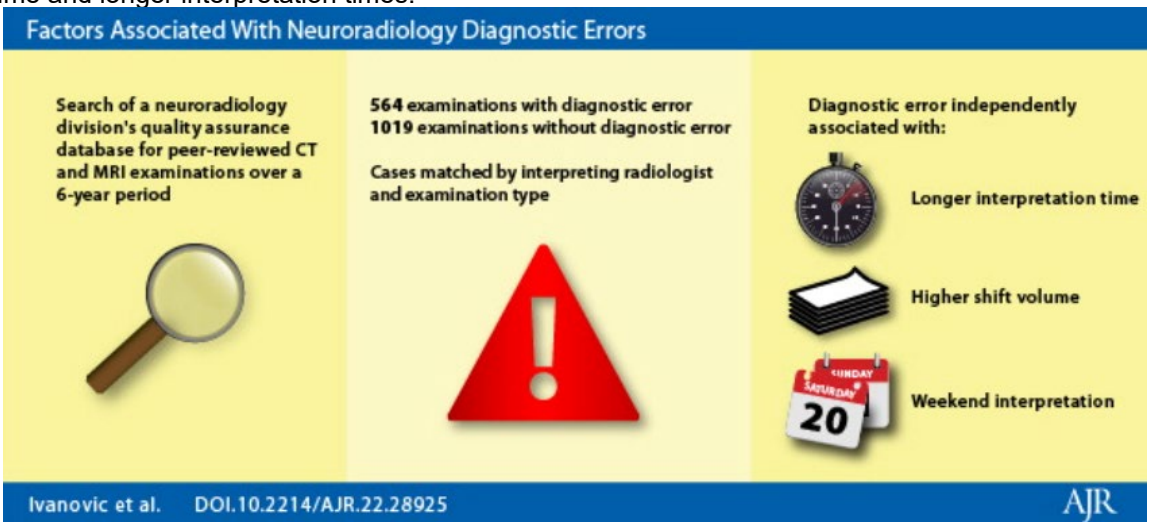

1. Ivanovic V, Broadhead K, Beck R, et al. Factors Associated With Neuroradiology Diagnostic Errors at a Large Tertiary-Care Academic Medical Center: A Case-Control Study. *AJR Am J Roentgenol* 2023 2023/03/30. DOI: 10.2214/ajr.22.28925.
2. Biddle G, Assadsangabi R, Broadhead K, et al. Diagnostic Errors in Cerebrovascular Pathology: Retrospective Analysis of a Neuroradiology Database at a Large Tertiary Academic Medical Center. *AJNR Am J Neuroradiol* 2022; 43: 1271-1278. 2022/08/05. DOI: 10.3174/ajnr.A7596.
3. Ivanovic V, Assadsangabi R, Hacein-Bey L, et al. Neuroradiology diagnostic errors at a tertiary academic centre: effect of participation in tumour boards and physician experience. *Clin Radiol* 2022 2022/05/20. DOI: 10.1016/j.crad.2022.04.006.
4. Ferguson A, Assadsangabi R, Chang J, et al. Analysis of misses in imaging of head and neck pathology by attending neuroradiologists at a single tertiary academic medical centre. *Clin Radiol* 2021; 76: 786.e789-786.e713. 2021/07/27. DOI: 10.1016/j.crad.2021.06.011.

Call Preparation for July 4th – A Case Series of Fireworks-Related Orbitofacial Trauma

Sean Boyle, M.D., *Arjun Vij, M.D., Matthew Bobinski, M.D., Ph.D., Arthur Dublin, M.D., Richard Latchaw, M.D., Arzu Ozturk, M.D., Osama Raslan, M.D., M.Sc., M.B.B.Ch., Maryam Shahrzad, M.D., Lotfi Hacein-Bey, M.D., H. Kader Karli Oguz, M.D.*

INTRODUCTION: There were approximately 10,200 fireworks-related Emergency Department visits nationwide in 2022 (1). Literature discussing the details of orbitofacial trauma in this setting is limited to case reports and a single clinical case series of 18 cases (2). Our goal is to further explore patterns of orbitofacial injuries identified on CT in this setting.

METHODS: CT examinations of the head and face with a provided history of fireworks injury were identified via a search of the institutional database. Cases without acute findings were excluded, yielding a total of 19 cases. Examinations were assessed for presence and type of orbitofacial injuries. Review of the EMR was also performed to assess for clinical information including corneal injury.

RESULTS: The most common orbitofacial injuries were periorbital edema/hemorrhage (68%), followed by facial fractures (42%), frank globe rupture (26%), nonorbital facial soft tissue injuries (21%) and lens dislocation (16%). Periorbital foreign bodies were noted in 9 cases (47%). Among the 14 cases without frank globe rupture, 7 (50%) had corneal injuries identified on ophthalmologic examination, including 6 corneal abrasions and 1 corneal thermal injury.

DISCUSSION: In cases with facial fractures, one or more of the orbital walls was involved in a majority (87.5%) of patients, with the medial wall being most common. Lens dislocations exclusively occurred in the absence of facial fractures or periorbital foreign bodies, with periorbital hemorrhage/edema being present in all cases. The most sensitive correlative CT finding for corneal injury was periorbital hemorrhage/edema (present in 6 of 7 cases).

CONCLUSION: CT examinations of the face with a history of fireworks injury should prompt a detailed search of the orbital structures. Presence of periorbital edema should prompt ophthalmologic evaluation if not already obtained as the incidence of corneal injury in these patients is high.

Case	Age	Gender	Globe rupture	Lens dislocation	Facial fractures	Periorbital hemorrhage/edema	Non-orbital facial soft tissue injury	Periorbital FB	Other Facial FB	Corneal injury
1	58	Male	Yes	No	Yes	Yes	No	Yes	No	-
2	17	Male	No	Yes	No	Yes	No	No	No	Yes
3	21	Male	No	No	Yes	Yes	No	Yes	No	Yes
4	25	Female	No	No	No	No	Yes	No	No	No
5	44	Male	No	No	No	No	Yes	No	Yes	No
6	14	Male	No	No	Yes	Yes	No	Yes	No	Yes
7	25	Male	No	No	No	No	No	Yes	No	No
8	30	Male	No	No	Yes	Yes	No	Yes	No	No
9	67	Male	No	Yes	No	Yes	No	No	No	Yes
10	12	Male	No	No	No	No	Yes	No	Yes	No
11	20	Male	Yes	No	Yes	Yes	No	Yes	No	-
12	10	Male	No	No	No	No	Yes	No	No	No
13	28	Male	Yes	No	Yes	Yes	No	No	No	-
14	18	Male	No	Yes	No	Yes	No	No	No	No
15	15	Male	No	No	Yes	No	No	No	Yes	Yes
16	18	Male	No	No	No	Yes	No	Yes	No	Yes
17	31	Female	Yes	No	Yes	Yes	No	Yes	No	-
18	41	Male	Yes	No	No	Yes	No	Yes	No	-
19	53	Male	No	No	No	Yes	No	No	No	Yes
Total			5	3	8	13	4	9	3	7

Figure 1 Demographics and Characteristics of Orbitofacial Injuries from Study Examinations

1. Smith B, Pledger D. 2022 Fireworks Annual Report Fireworks-Related Deaths, Emergency Department Treated Injuries, and Enforcement Activities During 2022. Published online June 2023. Accessed July 2, 2023. https://www.cpsc.gov/s3fs-public/2022-Fireworks-Annual-Report.pdf

2. Yi Y. CT Findings of Firework Injuries to the Head and Neck. Ginat D, ed. Ear, Nose & Throat Journal. Published online 2021.

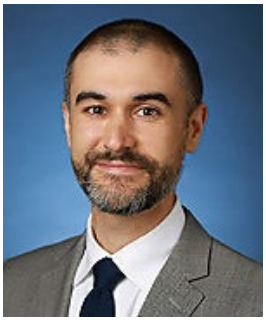

Prevalence of Malignancy among Incidentally Detected Hyperechoic Liver Lesions on Ultrasound in Patients Without Known Malignancy or Liver Disease

Authors: **Carney BW**, Hansra SS, Choudhury LS, Corwin MT

Introduction: While the majority of incidental liver lesions can be diagnosed using US characteristics alone, hyperechoic liver lesions often present a diagnostic dilemma as they can arise from both benign and malignant entities. This fact can lead to unnecessary additional imaging. We sought to determine the prevalence of malignancy among incidental hyperechoic liver lesions detected on ultrasound in patients without cancer or chronic liver disease.

Methods: Retrospective search of ultrasound reports to identify hyperechoic liver lesions in patients without a history of malignancy or chronic liver disease. Lesions were included if they had one of two typical appearances of hemangiomas (homogeneously hyperechoic or hypoechoic/isoechoic with hyperechoic rim. Presence of internal vascularity and background steatosis was also assessed. The reference standard for benignity was CT/MR diagnostic of hemangioma (n=54), imaging stability on follow-up ≥ 1 year (n=66), or clinical follow-up ≥5 years showing no evidence of malignancy (n=18). The binominal exact calculation was used to determine the one-sided 95% confidence interval.

Results: There were no malignant masses (0/138; 0%, 95% CI 0.0-2.1%). There were 125 homogeneously hyperechoic lesions and 13 isoechoic/hypoechoic lesions with hyperechoic periphery. The mean lesion diameter was 18 mm (SD, 13 mm). 12 of the lesions demonstrated internal vascularity while 126 did not. Background steatosis was present in 3 patients and absent in 135 patients.

Discussion: Incidental hyperechoic liver lesions with typical hemangioma appearance on ultrasound in patients without cancer or chronic liver disease are highly likely benign.

Conclusion: Our study supports limited prior literature that suggests no follow-up imaging is appropriate for hyperechoic lesions in patients without cancer or liver disease. We hope our study reduces unnecessary follow-up imaging.

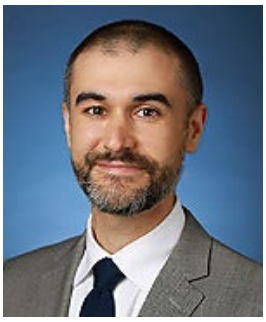

Utility of combined gadoxetic acid and ferumoxytol-enhanced liver MRI for preoperative detection of colorectal cancer liver metastases: a pilot study

Carney BW, Gholami S, Fananapazir G, Sekhon S, Lamba R, Loehfelm TW, Wilson MD, Corwin MT.

Background: Colorectal cancer (CRC) is the second-leading cause of cancer-related death worldwide and resection of CRC metastases confined to the liver is the treatment of choice when feasible. Ferumoxytol is an off-label contrast agent that opacifies vasculature and may be helpful in distinguishing metastases from small hemangiomas and blood vessels on gadoxetic acid-enhanced magnetic resonance imaging (MRI).

Purpose: To compare the diagnostic accuracy of MRI using a standard gadoxetic acid protocol and a combined gadoxetic acid/ferumoxytol protocol in patients with suspected colorectal hepatic metastases.

Material and methods: In this institutional review board-approved, single-institution, retrospective study, eight patients underwent gadoxetic acid-enhanced liver MRI, supplemented with additional T1-weighted ferumoxytol enhanced sequences. Two radiologists in consensus identified all metastases using all available sequences, which served as the reference standard. Two different radiologists reviewed each exam twice, once using the standard protocol and once with additional ferumoxytol sequences. The detection rate was estimated as the predicted probability of a metastasis along with the 95% confidence interval (CI) using hierarchical logistic regression models.

Results: A total of 49 metastases were identified. The mean diameter was 10 mm, measured in greatest axial dimension (median=7 mm; range=2-70 mm). Readers 1 and 2 had detection rates of 69.6% (95% CI = 48.2-85.0) and 53.1% (95% CI = 35.2-70.3) for gadoxetic acid alone and 98.0% (95% CI = 86.3-99.7) and 83.5% (95% CI = 59.3-94.7) for combined protocol.

Conclusion: In this preliminary investigation, adding ferumoxytol-enhanced sequences to gadoxetic acid liver MRI protocol increased the detection rate of CRC hepatic metastases and may aid in preoperative decision making.

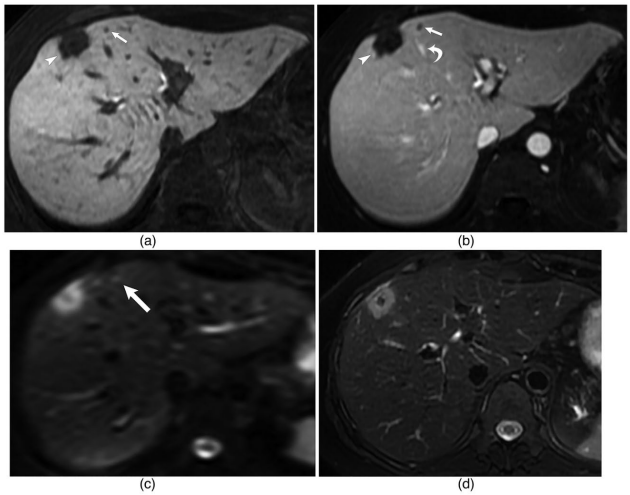

Fig. 2. A 60-year-old woman with a history of metastatic colon cancer: (a) 0.5 cm segment 4a lesion on 19 min delayed hepatobiliary phase gadoxetic acid alone sequence and (b) combined ferumoxytol-gadoxetic acid sequence. (c) The lesion is vaguely present on diffusion-weighted imaging, but much less conspicuous. (d) There is no correlate on T2-weighted imaging. Both readers identified the lesion on the combined sequence and failed to identify the lesion on the gadoxetic alone sequence (long arrows). A 2.3-cm metastasis immediately adjacent is easily identified on both sequences (arrowhead). Note the enhancement of a middle hepatic vein branch (curved arrow).

A Multi-Reader, Multi-Case Study Comparing Ultra-High-Resolution and Normal-Resolution CT for Lung Nodule Characterization

Anthony F. Chen, *Fatma Sen, Ana Mitchell, Sarah E. McKenney, Lorenzo Nardo, Ahmadreza Ghasemiesfe, Craig K. Abbey, Mohammad H. Madani, Andrew M. Hernandez*

Purpose: This study evaluates the efficacy of high-resolution CT (UHRCT) versus normal-resolution (NR) CT for characterization of lung nodules.

Methods: 104 non-contrast chest UHRCT scans with pulmonary nodules were collected, and NR reconstructions were synthesized with a validated algorithm. An experienced cardiothoracic radiologist first characterized each nodule, followed by four blinded radiologist readers given randomly distributed HR and NR datasets. Nodule characteristics used for scoring included: size (two dimensions), image quality (3-point Likert scale), margin clarity (5-point scale), density, and density confidence (0-100%). In-house 3D visualization software was used for reader scoring and to display a spherical VOI with the nodule. Image noise was calculated from a VOI within the trachea.

Results: Inter-reader agreement was excellent for long (ICC > 0.947) and short (ICC > 0.924) dimension assessment, and fair for margin clarity (k = 0.123 and 0.287 for NR and UHR, respectively) and overall image quality (k = 0.037 and 0.214 for NR and UHR). Margin clarity was rated significantly higher for UHR than for NR (3.7>3.4, p=0.002). Image quality was higher for UHR than for NR but not significantly (2.6>2.2, p=0.381). Nodule density was correctly scored for 50% of each UHR and NR dataset, and for correctly scored cases the confidence was higher with UHR, but not significantly (92%>88%, p=0.124). No significant differences were observed in the bias associated with the short and long axis nodule measurements between readers with biases of 1.43-1.49 mm. The average image noise was 58.5 HU for NR and 61.4 HU for UHR.

Conclusion: UHRCT demonstrated an improved ability to visualize margin clarity. Additionally, readers found UHR image quality higher and had greater confidence in scoring nodule density, though not to a statistically significant extent. Improved margin clarity with UHRCT may help more accurate characterization of lung nodules.

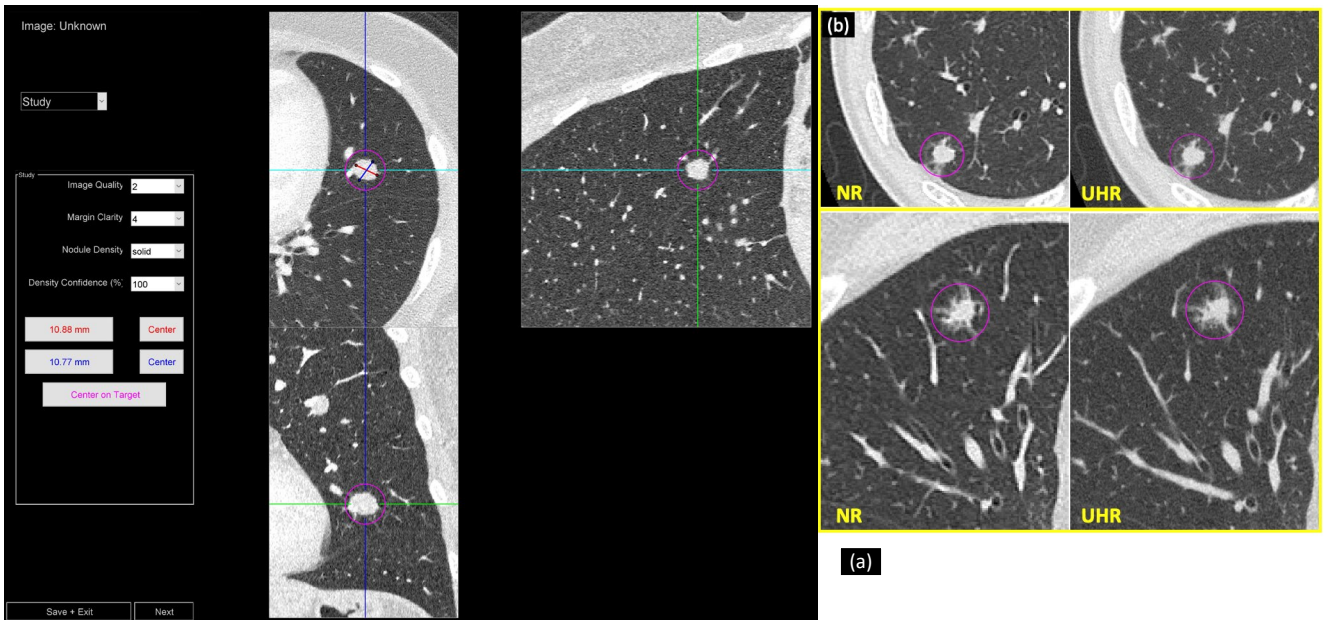

Figure 1. Custom built visualization software used for the study including a GUI for scoring the nodule characteristics (a). Two examples of spiculated nodules in normal resolution (NR) and high resolution (UHR) images (b). All images were reconstructed using an iterative reconstruction algorithm and a lung kernel. The UHR data was reconstructed into a voxel size of 0.3125 x 0.3125 x 0.250 mm. The NR data was reconstructed into a voxel size of 0.625 x 0.625 x 0.500 mm.

Intra-articular injections of the foot: An evaluation of physician ordering practices of ketorolac and Kenalog

Authors: **Justin Choi**, David S Chen, Jasjeet Bindra

Introduction: Intra-articular steroid injections provide therapeutic relief and diagnostic evaluation of foot pain. Nonsteroidal anti-inflammatory injectants may offer a safer profile and have been shown to provide similar levels of pain relief as steroids. This study sought to evaluate physician preferences for injection agents for intra-articular foot injections.

Methods: An IRB-approved retrospective review was performed using radiology data mining system (Nuance mPower) to identify patients who received foot injections from 2011-2023 at a single academic institution. Study participants were eligible if they received an image-guided foot injection and divided into two cohorts: 1) injection with Kenalog and 2) injection with ketorolac. Demographics, diagnosis, site, agent, treatment history, and ordering provider were recorded. Categorical variables were compared using Pearson's chi-square test.

Results: Forty one of the 182 injections were with ketorolac. Eighty four percent of the patients were female and the average age was 65.5 years-old. Osteoarthritis was the most common diagnosis for Kenalog and ketorolac injections (95% and 51%, respectively, $p<0.01$) while the tarsometatarsal joints were the most common sites for both cohorts (82% and 37%, respectively, $p<0.01$). Of the four physicians identified, Physician 1 ordered ketorolac for 85% of the injections and Physician 2 ordered Kenalog for 91% of the injections ($p<0.01$). Twenty one percent of cohort 1 and 34% of cohort 2 underwent surgery after injections ($p=0.26$).

Discussion: There was a clear preference in the agent ordered by each physician without a significant difference in post-injection surgical treatment rates. In recent years, there was an increase in usage of ketorolac and for a wider range of sites and diagnoses compared to Kenalog. Future studies could quantitate efficacy of intra-articular injections for foot pain by injectant.

Conclusion: Ketorolac is a low-cost option for diagnostic and therapeutic intra-articular injections of the foot that offers a safety profile comparable to steroids, without significant differences in outcomes.

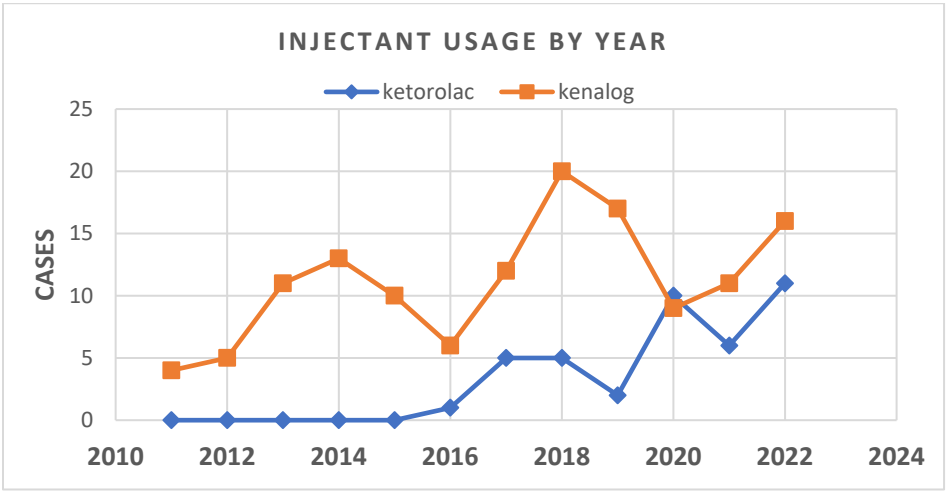

Figure 1. Data gathered from injection orders during 2011 to 2022 shows increasing usage of ketorolac as an injection agent beginning in 2016.

Quantifying the Blood-brain Barrier Permeability of Positron Emission Tomography Radiotracers

Kevin J. Chung,[1] Yasser G. Abdelhafez,[1] Benjamin A. Spencer,[1,2] Terry Jones,[1] Ramsey D. Badawi,[1,2] Simon R. Cherry,[1,2] Guobao Wang[1]

[1]Department of Radiology, University of California Davis Medical Center, Sacramento, CA
[2]Department of Biomedical Engineering, University of California Davis, Davis, CA

Introduction: Blood-brain barrier (BBB) dysfunction is implicated in many brain diseases. However, in-vivo methods to characterize BBB permeability are limited. Permeability can be quantified by kinetic modeling of dynamic contrast-enhanced CT or MRI, but these only reflect gross leakage of contrast rather than of specific molecules. We aimed to estimate the molecular BBB permeability to a radiotracer via time-varying kinetic modeling of high temporal resolution dynamic PET data that become possible on high-sensitivity scanners.

Results: The proposed method resolved substantial differences in the extravascular signal between the three radiotracers owing to their different BBB permeabilities. Across all included subjects, average ± standard deviation of CBF in the grey matter, white matter, and cerebellum were 0.591 0.123, 0.195±0.035, and 0.518±0.082 ml/min/cm^3, respectively, with low variation between radiotracers. Average whole brain PS was 0.016±0.003 and 0.130±0.009 ml/min/cm^3 for ^{18}F-fluciclovine and ^{18}F-FDG, respectively, and was indeterminately high as expected for ^{11}C-butanol.

Conclusion: BBB permeability differs among PET radiotracers and could be quantified using our proposed method. This may have significant clinical implications for characterizing tracer-specific BBB dysfunction in neurodegeneration and other brain disorders.

NOTE: The full abstract of this work is unavailable in this booklet. Please contact the authors for more information if you are interested.

Region-dependent kappa opioid receptor binding in a monkey model of social buffering and separation

Alita Jesal D'Almeida[1,2], Brad A. Hobson[3], Sarah Tam[3], Claudia Manca[4], John P. Paulus[4], Karen L. Bales[4,5] and Abhijit J. Chaudhari[2,3,5]

[1]Biomedical Engineering; [2]Radiology; [3]Center for Molecular and Genomic Imaging; [4]Psychology, [5]Neuroscience, University of California, Davis; [5]California National Primate Research Center

Introduction: Alterations in kappa opioid receptor (KOR) activity play an important role in the context of social separation and grief. Yet, there are limited data assessing these KOR fluctuations. Titi monkeys; a socially monogamous new-world species that exhibit signs of adult pair-bonding, present unique experimental models for understanding the role of KORs in this context. Therefore, we tested the following hypotheses: the uptake of the PET radiotracer [^{11}C]GR103545, targeted towards KORs, in the titi monkey brain is (1) consistent with that reported for other non-human primates (NHPs) and humans; and (2) altered by pretreatment by a KOR antagonist or agonist.

Methods: Adult titi monkeys (N=6) underwent [^{11}C]GR103545 PET brain scans (injected dose 37MBq/kg) at baseline, and PET scans after the administration of a KOR antagonist (LY2456302; 0.3mg/kg) and a KOR agonist (U50,488; 3mg/kg). Motion-corrected PET images had a voxel size of 0.8x0.8x0.8mm. To facilitate anatomical segmentation, brain MRI data were obtained (voxel size 0.3x0.3x1.0mm). Region-specific, non-displaceable binding potential (BP_{ND}) was calculated using (1) Simplified Reference Tissue Model 2 (SRTM2), and (2) Logan Reference Model (LRM), each using the cerebellum as the reference region. Primary analysis included 7 volumes of interest (VOIs) implicated in social connectedness (Figure 1B).

Results and Conclusions: BP_{ND} values across VOIs from baseline scans were consistent with those reported in other NHP and human studies. The pituitary gland showed the highest binding (BP_{ND} = 2.0 [1.36-2.2]). Compared to baseline, pretreatment with LY2456302 significantly reduced binding across all VOIs (77.3% reduction, $p<0.05$) while a region-dependent reduction of 10.6% was observed after U50,488 pretreatment. There was a high correlation between BP_{ND} assessed from SRTM2 and LRM (r_s=0.9936, $p<0.05$). This first study examining KOR activity in titi monkeys using PET lays the foundation for further experiments to analyze KOR binding dynamics longitudinally and in a post-intervention setting.

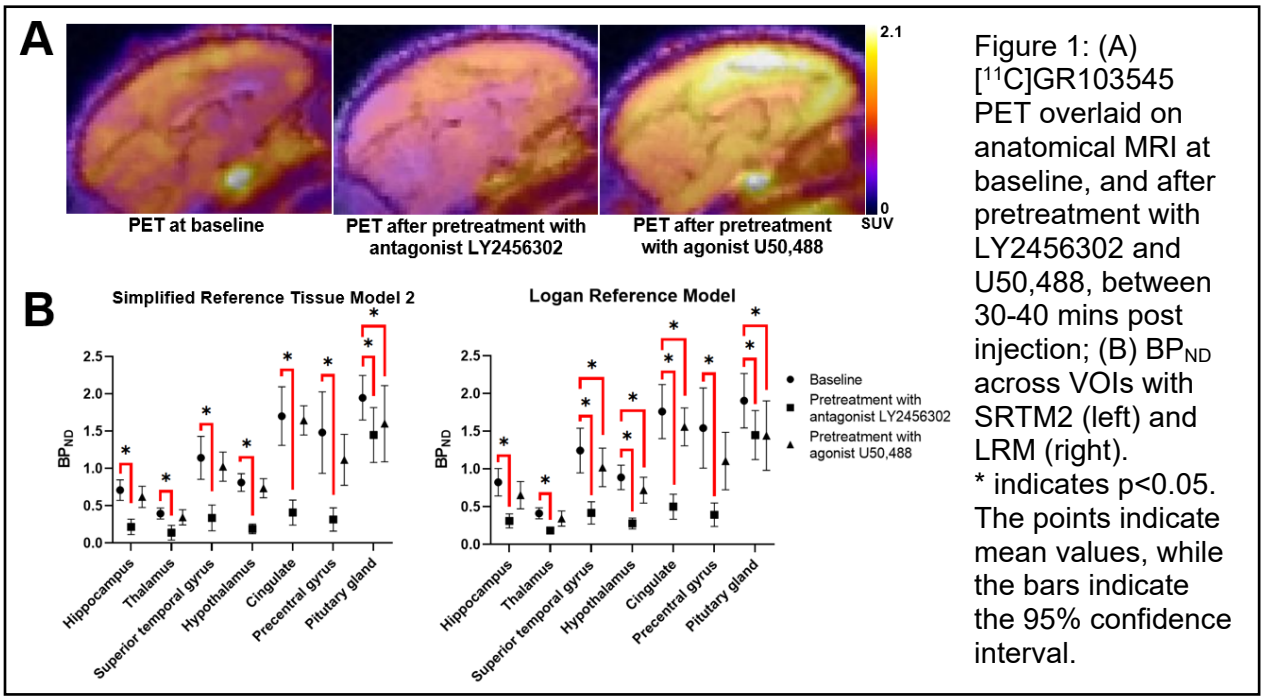

Figure 1: (A) [^{11}C]GR103545 PET overlaid on anatomical MRI at baseline, and after pretreatment with LY2456302 and U50,488, between 30-40 mins post injection; (B) BP_{ND} across VOIs with SRTM2 (left) and LRM (right). * indicates $p<0.05$. The points indicate mean values, while the bars indicate the 95% confidence interval.

Quantification of Liver ^{18}F-FDG Delivery Rate Using a Shortened Dynamic PET Scan in Nonalcoholic Fatty Liver Disease

Xiaoyu Duan[1], Souvik Sarkar[1], Michael Corwin[1], Ramsey D. Badawi[1,2], Guobao Wang[1]

[1]Department of Radiology, University of California Davis Medical Center [2]Department of Biomedical Engineering, University of California, Davis

Introduction: Nonalcoholic steatohepatitis (NASH) is a more severe form of nonalcoholic fatty liver disease (NAFLD) and affects a large population in US. A hallmark for detecting NASH from NAFLD is liver inflammation, for which there is currently no imaging method in the clinic. We have developed a parametric ^{18}F-FDG PET method that uses dynamic PET and tracer kinetic modeling to measure the liver FDG delivery rate K_1 as a potential biomarker for liver inflammation. However, the current method requires one hour scan, which hinders its practical clinical use. In this study, we investigate the feasibility of a shortened dynamic scan duration without compromising FDG K_1 quantification in liver.

Methods: 44 patients with NAFLD had a one-hour dynamic ^{18}F-FDG PET scan on a GE Discovery 690 PET/CT scanner. The average of eight segment regions of interest (ROIs) on liver was used as a whole ROI to extract global liver time activity curves (TACs). A reversible two-tissue compartment model with an optimized dual-blood input function was used to fit the TACs and estimate liver FDG kinetics (Figure 1A). Different shortened scan durations, ranging from 5-45 minutes, were compared to the full scan duration 60 minutes using the Pearson's correlation analysis (Figure 1B). Practical identifiability analysis was also conducted with computer simulation to evaluate the bias, standard deviation (SD) and root mean square error (RMSE) of liver FDG K_1 estimation with different scan durations (Figure 1C).

Results: Bias and RMSE decreased with scan time increased and had a sharp decrease trend after 10min. SD was 6.5% at 15min and decreased at 5.9% at 60min. The correlation of K_1 between 15min and 1h was stronger than it between 10min and 1h.

Discussion and Conclusion: Simulation results demonstrated that K_1 estimation from a 10-15min scan is reliable. Clinical studies further indicated 15min agrees better with that from 1h dynamic scan. Future work will investigate whether 15min derived K_1 is associated with liver inflammation biopsy results.

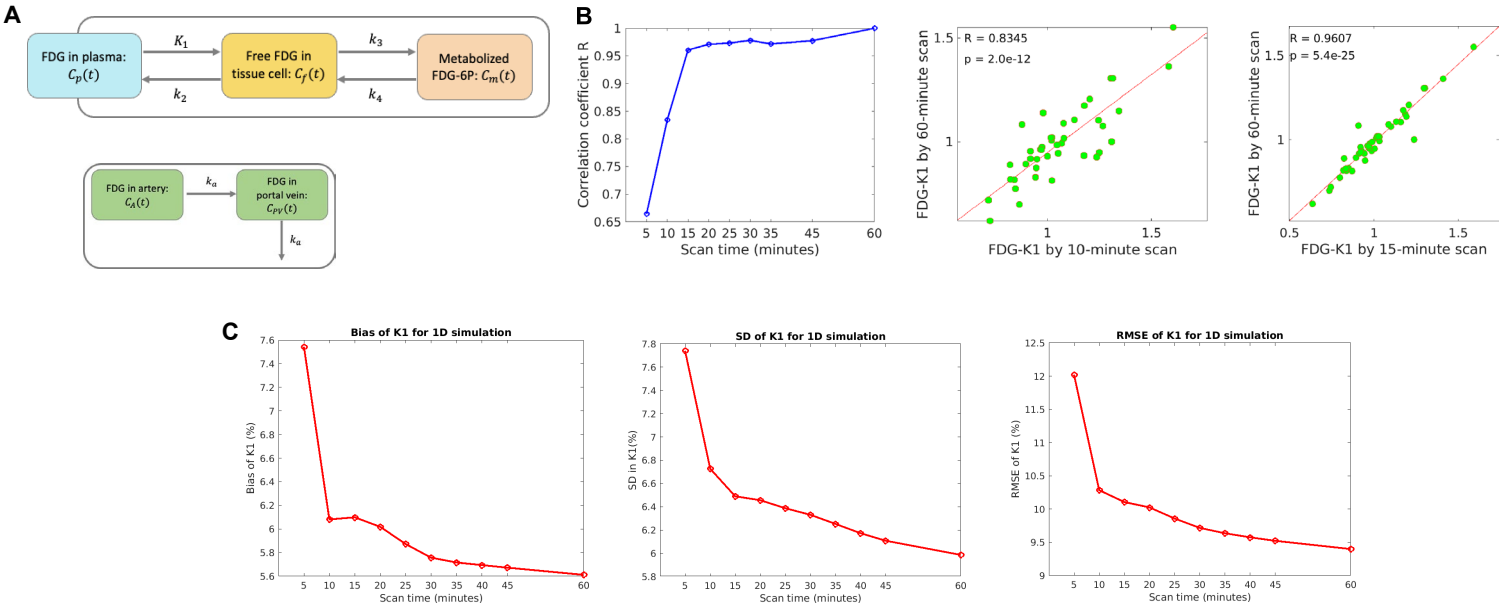

Figure 1A. Kinetic modeling of dynamic PET with a dual-blood input function. B. Pearson's correlation with different scan duration in 44 patients. C. Bias, SD and RMSE of liver FDG K_1 for 1D computer simulation.

First-in-human study of the theranostic pair [^{68}Ga]Ga DOTA-5G and [^{177}Lu]Lu DOTA-ABM-5G in pancreatic adenocarcinoma

Authors: Ryan A. Davis[1], **Cameron C. Foster[2],** Tanushree Ganguly[1], Sven H. Hausner[3], Edward J. Kim[4], Emilie Roncali[2] and Julie L. Sutcliffe[1,3, 4].

Affiliations: 1. Department of Biomedical Engineering, 2. Department of Radiology, 3. Division of Hematology/Oncology, Department of Internal Medicine, 4 Center for Molecular and Genomic Imaging.

Introduction: This is a Phase I, first-in-human study to evaluate the safety of the radiotheranostic peptide pair, [^{68}Ga]Ga DOTA-5G and [^{177}Lu]Lu DOTA-ABM-5G in patients with locally advanced or metastatic pancreatic adenocarcinoma (PDAC). PET/CT imaging with [^{68}Ga]Ga DOTA-5G is being used diagnostically to select patients that have $\alpha_v\beta_6$-avid disease who are then be eligible for treatment with the [^{177}Lu]Lu DOTA-ABM-5G. SPECT/CT imaging is being used to quantify the whole body dosimetry for the [^{177}Lu]Lu DOTA-ABM-5G.

Methods: Patients received an intravenous injection (IV) of up to 5 mCi of [^{68}Ga]Ga DOTA-5G; PET/CT images were acquired 1 and 2 hours post injection (p.i.) Patients with lesions with an SUV_{max} ([^{68}Ga]Ga DOTA- 5G) >2-fold above normal lung, or liver were eligible for [^{177}Lu]Lu DOTA-ABM-5G treatment. Eligible patients received a single treatment with [^{177}Lu]Lu DOTA-ABM-5G (25-150 mCi, 3+3 dose escalation) and underwent whole body planar imaging (anterior and posterior view) and SPECT/CT imaging at approximately 1 and 7-days following administration of [^{177}Lu]Lu DOTA-ABM-5G, for evaluation of biodistribution and dosimetry. Organs-at-risk (kidneys, bone marrow) were contoured on CT to extract the Lu-177 activity and organ volume, which were used in OLINDA/EXM 1.1 to calculate the absorbed dose.

Results: To date, 17 patients have been imaged with [^{68}Ga]Ga DOTA-5G and 14 patients have been treated with [^{177}Lu]Lu DOTA-ABM-5G. Both agents were predominantly renally excreted, well tolerated and no drug related serious adverse events have been observed. Representative images shown in Figure 1. Currently patients are being enrolled for treatment at the maximum dose level of 200 mCi.

Conclusion: To date we have demonstrated that [^{68}Ga]Ga DOTA-5G PET can be used to visualize disease and select patients for treatment, that the [^{177}Lu]Lu DOTA-ABM-5G reaches and is retained by the metastasis and that the theranostic pair [^{68}Ga]Ga DOTA-5G and [^{177}Lu]Lu DOTA-ABM-5G is safe and well tolerated.

Image

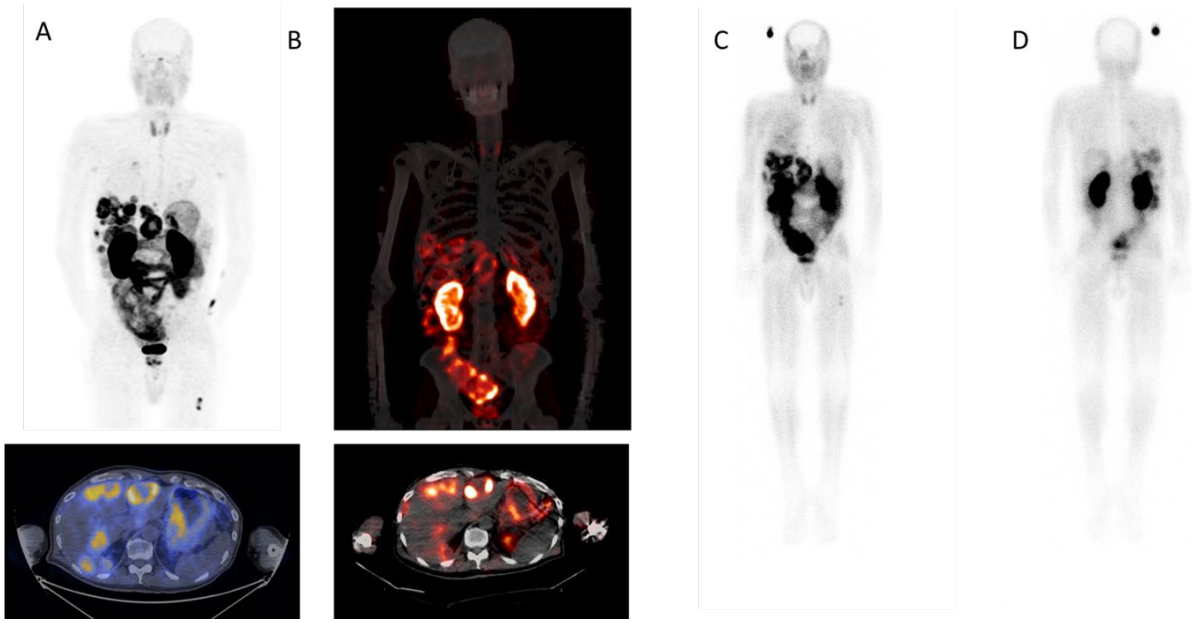

Figure 1: A. [^{68}Ga]Ga DOTA-5G PET/CT images (1 hour p.i.) **B.** [^{177}Lu]Lu DOTA-ABM-5G SPECT/CT images (1 day p.i.) **C.** [^{177}Lu]Lu DOTA-ABM-5G whole body planar image (anterior, 1 day p.i.), and **D.** [^{177}Lu]Lu DOTA-ABM-5G whole body planar image (posterior, 1 day p.i.).

Simulation of the Electric Transfer Function of Partially Inserted Guidewires

Felipe Godinez[1,2], Jeff Hand[2], Özlem Ipek[2,3], Fatima Ben Haj[4], Joseph V Hajnal[2,3], Shaihan J Malik[2,3]

[1]Department of Radiology, University of California Davis, Sacramento, California, USA
[2]Biomedical Engineering Department, School of Biomedical Engineering and Imaging Sciences, King's College London, London, UK
[3]Centre for the Developing Brain, School of Biomedical Engineering and Imaging Sciences, King's College London, London, UK
[4]Davis Senior High School, Davis, California, USA

Introduction: The electric transfer function (TF) model can predict heating in lead wires of cardiac implants while in the MRI, however, a similar approach in guidewires is lacking. In practice guidewires are partially inserted to allow the operator to maneuver them. In this work we evaluated partially inserted guidewire using the TF approach.

Methods: In simulation, a 180cm long wire in a dielectric medium was excited at the tip with RF frequencies 23MHz, 64MHz, and 128MHz, corresponding to magnetic strengths of 0.55T, 1.5T, and 3T, respectively. It consisted of insulation, a 1mm diameter conductor with 10mm of the tip exposed. It was partially inserted into a rectangular phantom, with the insertion depth ranging from 100mm to 1100mm at 50mm intervals. The TFs for each case were computed compared in magnitude and phase.

Results: The TF magnitude and phase profiles are plotted in figure 1 for all insertion depths and frequencies. The TF profile changed significantly with insertion depth, the most extreme at 64MHz. The peak values were 19.2 m^{-1} at 250mm, 48.0 m^{-1} at 1500mm, and 2.4 m^{-1} at 450mm, for frequency 128MHz, 64MHz, and 23MHz respectively.

Discussion: We observed two related effects: (i) the 'shape' of the TF varies with insertion depth at all frequencies, the strongest at 64MHz (ii) the overall peak amplitude of the TF also varies with frequency and is also observed to be strongest at 64MHz. Strong phase variation of the TF is observed at the higher frequencies; this can lead to reduced total scattered E-fields at the tip since contributions from incident fields at different portions of the wire cancel each other out.

Conclusion: We have compared the TF for a range of insertion depths and frequencies and found it useful to predict the behavior of a partially inserted guidewires, as used in an interventional MR setting.

A

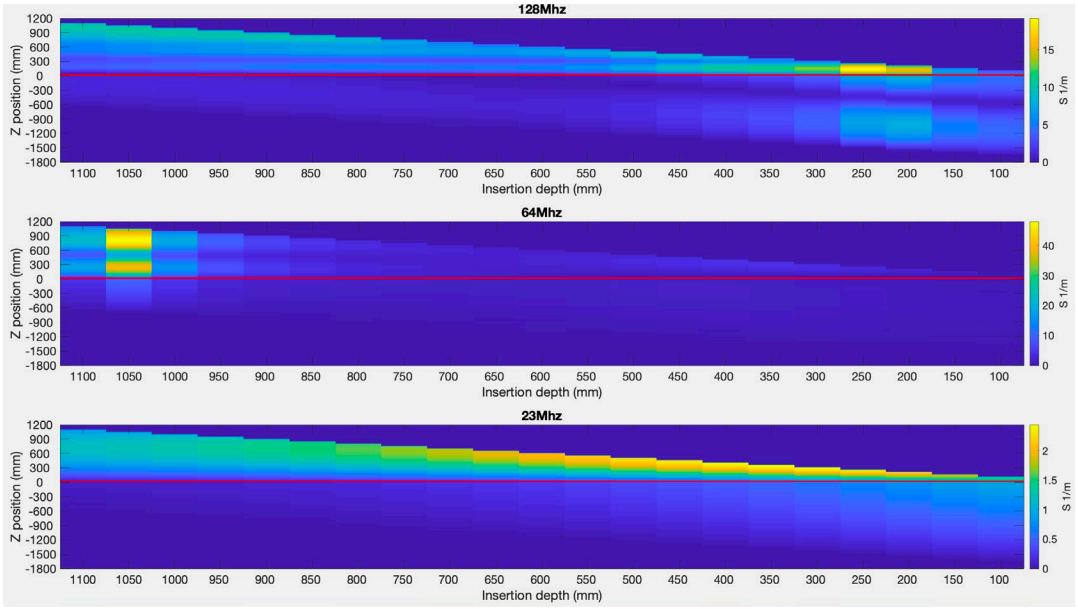

B

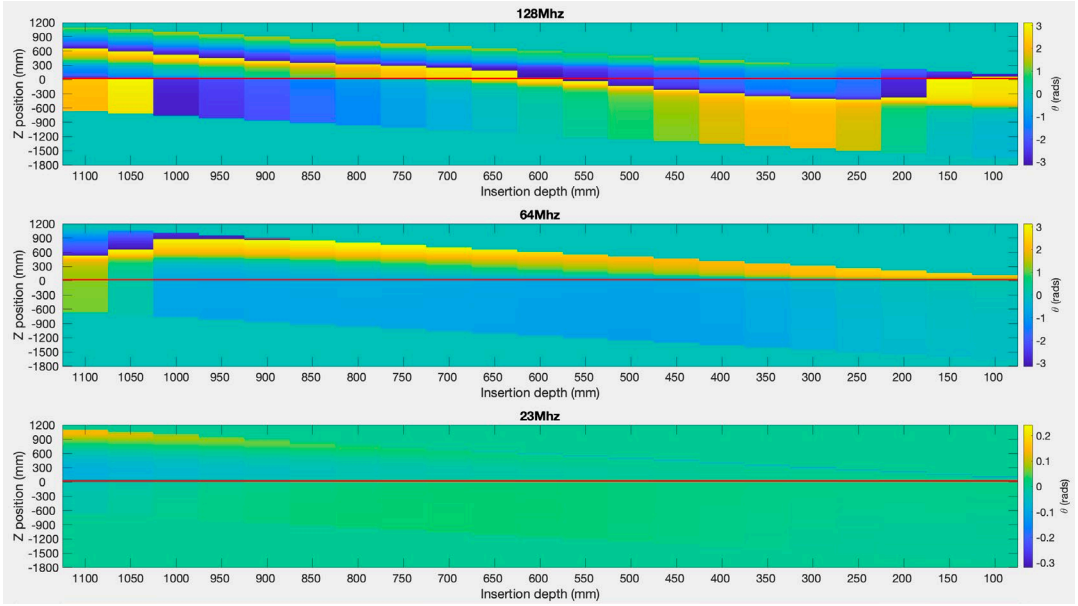

Figure 1. The transfer function magnitude (A) and phase (B) calculated for multiple frequencies, 128MHz, 64MHz, and 23MHz, corresponding to 3T, 1.5T, and 0.55T. The smallest values for the transfer function was at 0.55T and the highest TF was for 1.5T. The guidewire was most resonant at 1.5T. The redline indicates the insertion point at the phantom edge, z = 0mm. Note the color scales are different.

A Bayesian machine learning approach for predicting atypical lipomatous tumors from MR radiomics

Godinez F[1], Roy A[3], Abdelhafez Y[1], Yuan N[4], Ng Q[1], Bateni C[1],Qi J[4], Guindani M[2], Nardo L[1]

[1]Department of Radiology, University of California Davis
[2]Department of Biostatistics, University of California Los Angeles
[3]The Indian Statistical Institute, Kolkata, India
[4]Department of Biomedical Engineering, University of California Davis

Introduction: Atypical lipomatous tumors (ALTs) are hard to differentiate from simple lipomas on MRI and an excision biopsy is frequently required to establish this distinction. Only complete surgical resection and pathologic examination of the entire lesion are able to provide a definite diagnosis. Here we explore a non-invasive way to perform diagnosis using machine learning (ML) approach. The aim is to benchmark the classification performance of ALT predictor model-based ML with Bayesian additive regression trees (BART) driven by MRI radiomics.

Methods: At a single institution, T1-MRI images were collected from 229 patients with suspected ALT, an excisional biopsy (including MDM2 analysis) confirmed the diagnosis of either ALT or simple lipoma. A total of 1132 radiomics features were extracted from each image using the pyRadiomics software. The ML model was implemented using the BARTmachine tool. The ML was benchmarked using data subsets for training (70%) and testing (30%). Based on the BART output confusion matrix, the sensitivity, specificity, accuracy, false positive rate, misclassification rate, positive predictive value, and negative predictive value were computed. The process was repeated 500 times to generate statistical metrics.

Results: The result for the performance metrics are shown in table 1. The accuracy using the data subsets for training and testing was, 0.84 (SD=0.04) for the BART model.

Discussion: The aim of this work is to distinguish benign lipomas from well differentiated liposarcomas using an ML model. Given the current performance, this prediction might be used to inform the radiologist's decision, especially with equivocal readings, thus improving overall accuracy. In future work, we would like to determine the effect of individual features on the model performance, for the refinement of the model and the impacts of multi-institution data sets.

Conclusion: The BART machine learning model is capable of accurately classifying ALTs from simple lipomas.

Table 1 Performance metrics for all features included.

	70%/30% training/testing
Measure	BART (mean/SD)
Sensitivity	0.890/0.048
Specificity	0.743/0.0828
Accuracy	0.835/0.0390
False Positive Rate	0.257/0.0828
Misclassification rate	0.165/0.0390
Positive predictive value	0.855/0.0393
Negative Predictive value	0.807/0.0694

Decreased Size of Diaphragm Hiatus Following Percutaneous Gastrostomy Tubes: An Unintended Benefit?

Shan S. Hansra M.D., Arjun Vij M.D., Brandon M. Wong, Michael C. Larson M.D. Ph.D.

INTRODUCTION: The incidence of hiatal hernia increases with age, with 1 out of every 13 retirement-age people having a symptomatic “sliding” hiatal hernia. Currently there are only two options for sliding hiatal hernia symptom relief: indefinite medication use or invasive surgery.
We hypothesize that gastropexy (anchoring the stomach to the abdominal wall) could serve as a potential treatment for symptomatic hiatal hernias by preventing the stomach from sliding through the diaphragm. Gastropexy is performed as part of the stomach feeding tube (gastrostomy or G-tube) procedure by interventional radiology.

METHODS: We used Nuance® mPower™ Clinical Analytics to perform a sequential search to find all patients who had a CT with mention of a “hiatal hernia” before having a G-tube placed over the 6-year period between 1/1/2015 and 12/31/2020.

Our sample contained 37 patients after applying the exclusion criteria (those with failed G-tube placement, without any follow-up CT, or obscured hiatus on follow-up CT).
The largest width of the diaphragm hiatus was measured on axial plane from CTs performed before and after G-tube placement by 2 radiology residents, and average of the 2 used for comparison.

RESULTS: There was a significant decrease in hiatal hernia size following IR placed G-tubes, from a mean 18.4mm to 16.7mm.

DISCUSSION: This is the first study to assess the effect of gastropexy and G-tube placement on diaphragm hiatus size in those with *a priori* mention of hiatal hernia in their clinical CT report. Whether or not this addresses hiatal hernia symptoms needs to be evaluated.

CONCLUSION: Gastropexy may be a viable alternative to treat symptomatic sliding hiatal hernias. Further research is needed to assess if this unintended benefit of gastropexy should be considered an alternative to indefinite antacid medication use and invasive surgery.

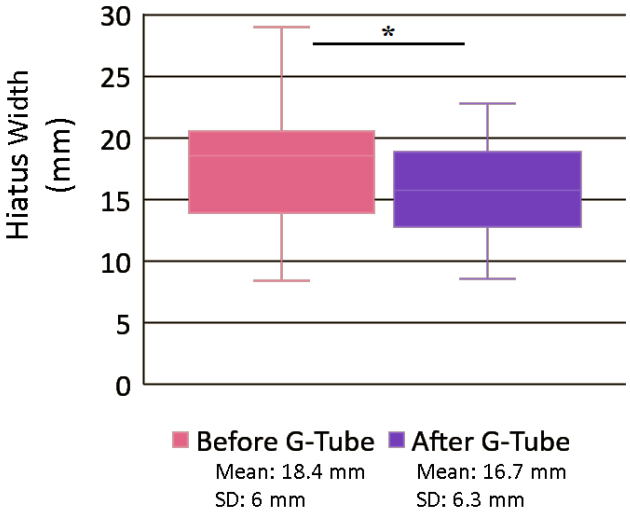

Figure: Diaphragm hiatus width before and after G-tube placement. The average hiatus width was 18.4 mm before G-tube placement (pink box) and 16.7 mm after G-tube placement (purple box).
*Paired 2-tailed t-test p-value 0.004.

Comparing the imaging performance of contrast-enhanced breast CT and breast MRI for BI- RADS 4 and 5 lesions

***Andrew M. Hernandez**, Su Hyun Lyu, George K. Burkett, Stephen Vong, Anthony Ronco, Shannon Navarro, Elizabeth A. Morris, Craig K. Abbey, John M. Boone, and Shadi Aminololama-Shakeri*

Introduction: To compare the diagnostic performance of contrast-enhanced breast CT (CEbCT) with contrast- enhanced breast magnetic resonance imaging (MRI) for the evaluation of suspicious breast lesions.

Methods: In this IRB approved study we recruited 48 women, with a mean age of 59 years with BI-RADS 4 or 5 findings after conventional diagnostic workup. All patients had bCT and MRI examinations followed by core breast biopsy. The CEbCT exam was acquired on a prototype breast CT system after injection of iodine-based contrast. MRI exams were acquired on a 1.5T GE Optima 450W MRI system using established clinical protocols with injection of gadolinium-based contrast. Four radiologists with breast imaging subspecialty fellowship training reviewed the CEbCT and MRI exams for each patient using a 3D visualization software developed in-house. The exams were split and randomly assigned into two reading phases with a minimum interval of 4 weeks between each phase. Pre- and post-contrast images were displayed side-by-side for each modality. The readers were prompted to score the overall background parenchyma enhancement (BPE), localize and assign BI-RADS scores to all lesions, and estimate the probability of malignancy (POM) on a scale from 0 to 100%. The sensitivity, specificity, positive predictive value (PPV) and negative predictive value (NPV) were computed.

Results: The cohort consisted of 19 malignant and 29 benign lesions. For benign lesions, the BPE was significantly higher on MRI than CEbCT ($p<0.01$) and no significant differences were observed for malignant lesions. Averaged across all readers, the sensitivity was 91% for CEbCT and 93% for MRI with no significant differences observed ($p=0.717$). Specificity was significantly higher ($p<0.002$) for CEbCT (41%) than for MRI (24%). When averaged across all readers, the PPV was 53% (standard error = 3.2%) for CEbCT and 41% (1.6%) for MRI. However, this difference was not statistically significant ($p = 0.068$). The average NPV across all readers was 88% for CEbCT and 91% for MRI ($p = 0.666$).

Conclusion: Preliminary comparison of the diagnostic performance of CEbCT and MRI, showed the specificity of CEbCT to be significantly higher than MRI. BPE on MRI was also noted to be higher than CEbCT for benign lesions. No statistically significant differences in sensitivity, PPV, or NPV was demonstrated among the readers and patient cases examined. These findings suggest that CEbCT could potentially serve as a viable alternative imaging modality for diagnostic breast examinations.

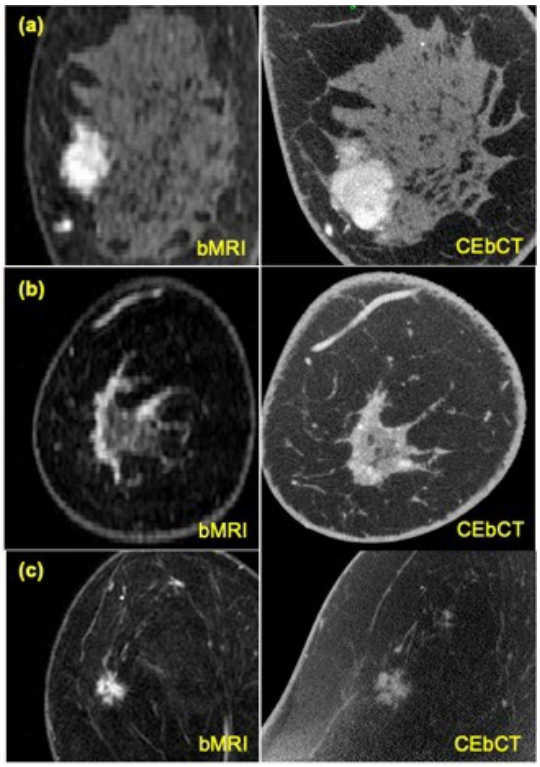

Figure 1. Patient examples of CEbCT and MRI images showing (a) an invasive mammary carcinoma in the coronal plane, (b) a benign lobular carcinoma in situ in the coronal plane, and (c) an invasive mammary carcinoma in the axial plane.

Improved Intensity Based WMH Detection Using a Ventricle Template and 3D Distant Calculation

Sarah Hong[1], Donghoon Kim[1,2], Arzu Ozturk[1], Sterling Johnson[3], Youngkyoo Jung[1]

[1]Department of Radiology, University of California Davis School of Medicine, Sacramento, CA
[2]Department of Biomedical Engineering, University of California Davis, Davis, CA,
[3]Wisconsin Alzheimer's Institute, University of Wisconsin School of Medicine and Public Health, Madison, WI

INTRODUCTION: Delineation of White Matter Hyperintensities is crucial in neurological research, but manual identification requires high level of expertise. Machine learning algorithms show promise in WMH detection (Park, 2021). However, they often struggle with large WMH because of limited training data. W2MHS is an automated WMH detection toolbox based on T1 weighted and T2 FLAIR intensities (Ithapu, 2014). Although successful in detecting large WMH lesions, improvements can be made in ventricle segmentation and 2D distance computation. We proposed a modified W2MHS with template-based ventricular detection and 3D distance computation and compared with widely used lesion segmentation algorithms.

METHODS: T1 weighted and T2 FLAIR images from six participants (60-75 yrs) with Fazekas scale of 1-3 were used to compare algorithms: modified and original W2MHS, LST3 (Schmidt et al., 2012), and U-Net with Multi-scale Highlighting Foregrounds (Park, 2021). The modified W2MHS employed a ventricle template warped to native space based on CAT12 and dilated by 3x3x3 voxels. The 3D distance was computed to reject a WMH close to GM and CSF. Dice coefficient and Hausdorff Distance were used as evaluation metrics.

RESULTS: The U-Net showed the highest DICE and the lowest HD for the scale of 1-2 while the modified W2MHS showed superior values for scale 3. Visual inspection revealed false positive WMH lesions in periventricular area for all algorithms except U-Net and modified W2MHS. The proposed algorithm missed some WMHs near GM due to 3D distance calculation unlike the original W2MHS. For scale 3, LST and U-Net detected only some parts of large WMH lesions, whereas both W2MHS algorithms provided more comprehensive segmentation.

CONCLUSION: The U-Net excels in detecting relatively small WMHs, while the proposed modified W2MHS algorithm is more suitable for detecting large WMHs, with a need for adjustments in distance thresholds to detect WMHs close to GM.

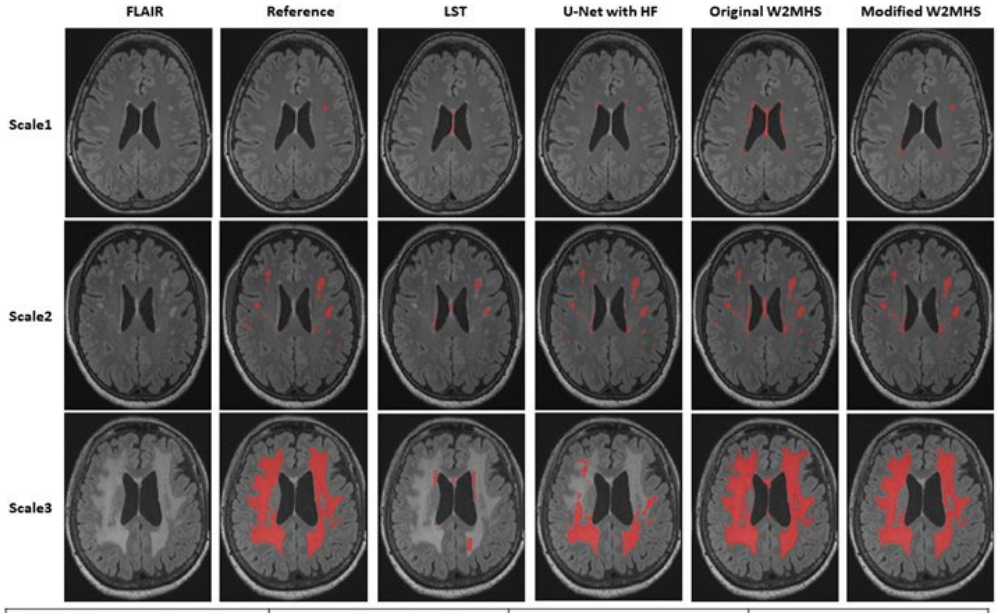

	Scale 1		Scale 2		Scale 3	
	DICE	HD	DICE	HD	DICE	HD
W2MHS (original)	0.13	41.02	0.36	29.35	0.63	28.41
Lesion Segmentation Tool	0.026	32.82	0.26	18.70	0.33	22.75
U-Net with Highlighting Foregrounds	0.34	30.86	0.59	11.49	0.70	11.13
W2MHS (modified)	0.18	34.15	0.46	17.70	0.75	9.03

Figure 1. Visual and Quantitative comparison of automated WMH detection algorithms. Representative participant and slices of each Fazekas scale are shown.

REFERENCE

Ithapu, V. (2014), 'Extracting and summarizing white matter hyperintensities using supervised segmentation methods in Alzheimer's disease risk and aging studies', Hum Brain Mapp., vol. 35, no. 8, pp. 4219-35.
Park, G. (2021), 'White matter hyperintensities segmentation using the ensemble U-Net with multi-scale highlighting foregrounds', NeuroImage, vol. 237, pp. 118140.
Schmidt, P. (2012), 'An automated tool for detection of FLAIR-hyperintense white-matter lesions in multiple sclerosis', Neuroimage, vol. 59, no. 4, pp.3774–3783

Sensitivity of MRI to detect microscopic fat in adrenal adenomas: Comparison of 2D dual gradient-echo and 3D DIXON techniques

Abdullah S. Khan, M.D.; Michael T. Corwin, M.D.

Introduction: We compare the sensitivity of 2D dual gradient-echo and 3D DIXON chemical shift MRI (CSI) for detecting microscopic fat in adrenal adenomas.

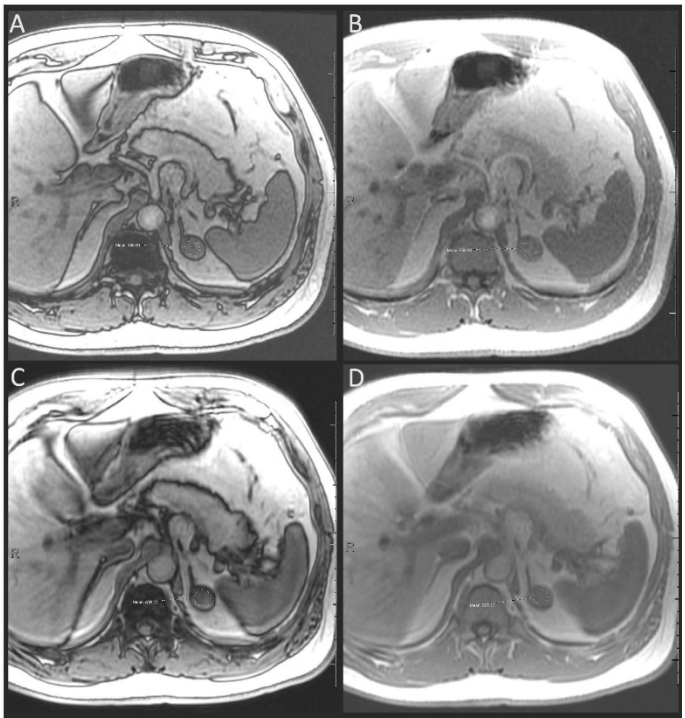

Figure 1. 56-year-old man with 2.2 cm left adrenal adenoma. Axial 2D dual gradient-echo T1-weighted images show mild loss of signal on the out of phase images (a) compared to the in phase (b) with a SII of 24.7%, compatible with an adenoma. Axial 3D DIXON T1-weighted images shows questionable minimal loss of signal on the out of phase (c) compared to the in phase (d) with a SII of 4.9%, which is indeterminate.

Methods: A retrospective study of 35 patients (15 male, mean age 61.8 years) with adrenal nodules underwent both 2D dual gradient-echo and 3D DIXON T1-weighted CSI. Signal intensity (SI) of the nodules was obtained using a replicable ROI and signal intensity index (SII) was calculated [100 x (SI in phase – SI out-of-phase)/SI in-phase]. Reference standard for the diagnosis of 29 adenomas was made by limited interval growth (<3mm/year, n=19), unenhanced CT attenuation of ≤ 10 HU (n=8), or pathology (n=2). One metastasis and one pheochromocytoma were diagnosed. Three nodules had no adequate reference standard. Sensitivity for the diagnosis of adrenal adenoma was determined using a SII of > 16.5%.

Results: There were 35 nodules (mean size 22 mm, range 11-55 mm). SII was higher on 2D CSI compared to 3D DIXON in 80% (28/35) of nodules by a mean of 14.4%. Of the 29 adenomas, the SII was higher on 2D CSI compared to 3D DIXON in 90% (26/29) of nodules, and mean SII was 48% on 2D CSI and 33% on 3D DIXON (p=.02). Sensitivity for the diagnosis of adenoma was 89.7% (26/29; 95% CI 72.7-97.8%) for 2D and 75.9% (22/29; 95% CI 56.5-89.7%) for 3D DIXON. None of the 3 non-adenomas had SII > 16.5% on either technique.

Discussion: 2D dual gradient-echo CSI has a higher sensitivity for detection of microscopic fat in adrenal nodules and the diagnosis of adrenal adenoma than the 3D DIXON technique. The sensitivity of 2D dual gradient-echo CSI for adrenal adenoma is approximately 90%.

Conclusion: Adrenal MRI protocols should include 2D dual gradient-echo CSI and not rely solely on 3D DIXON techniques for the diagnosis of adrenal adenomas.

Parametric Cerebral Blood Flow and Arterial Transit Time Mapping Using a Three-Dimensional Convolutional Neural Network

Donghoon Kim[1-2], Megan E. Lipford, Ph.D., [3] Hongjian He, Ph.D., [4] Qiuping Ding, M.S. [4] Vladimir Ivanovic, M.D., [5] Samuel N. Lockhart, Ph.D., [6] Suzanne Craft, Ph.D.,[6] Christopher T. Whitlow, M.D., Ph.D., [3] and Youngkyoo Jung, Ph.D.,[1-3]

[1]Department of Biomedical Engineering University of California Davis, California, USA
[2]Department of Radiology, University of California Davis, California, USA
[3]Department of Radiology, Wake Forest School of Medicine, Winston-Salem, North Carolina, USA
[4]Center for Brain Imaging Science and Technology, Zhejiang University, China
[5]Department of Radiology, Medical College of Wisconsin, Wisconsin, USA
[6]Department of Internal Medicine, Wake Forest School of Medicine, Winston-Salem, North Carolina, USA

Introduction: Multiple post labeling delays (PLD) arterial spin labeling (ASL) MRI has been used to estimate arterial transit time (ATT) and cerebral blood flow (CBF) more accurately with multiple PLDs than a single PLD. However, acquiring ASL images at multiple PLDs requires relatively longer scan time compared to a single PLD. The purpose of this study was to develop a deep learning-based algorithm to reduce the total scan time of multi- PLD pseudo-continuous ASL (PCASL).

Materials and Methods: A total of 48 subjects, 38 females and 10 males, aged 56-80 comprising a training group (n=45) and a validation group (n=3) underwent MRI including multi-PLD PCASL. We developed a hierarchically structured 3-dimensional convolutional neural network (H-CNN) to estimate the ATT and CBF maps using a reduced number of PLDs and a separately reduced number of averages[1]. The proposed method was compared to a conventional nonlinear model fitting method using the mean absolute error (MAE).

Results: The H-CNN provided the MAEs of 32.69 ms for ATT and 3.32 ml/100g/min for CBF estimations using a full dataset that contains 6 PLDs and 6 averages in the 3 test subjects. As shown in Figure 1, the H-CNN also showed that a smaller number of PLDs can be used to estimate both ATT and CBF without significant discrepancy from the reference (MAEs of 231.45 ms for ATT and 9.80 ml/100g/min for CBF using 3 PLDs out of 6 PLDs). Using the selected 3 PLDs offers a total scan time saving of 55.7 %.

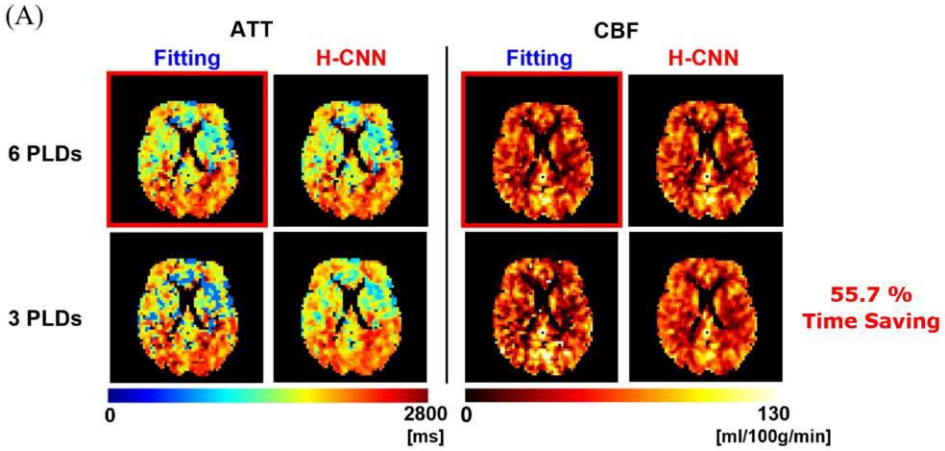

Figure 1. Estimated ATT and CBF maps from the nonlinear model fitting and H-CNN using the reduced number of PLDs. The ATT and CBF maps (red boxes) from the nonlinear model fitting with 6 PLDs and 6 Averages are the ground truth references of the subject.

Discussion and Conclusion: A smaller number of PLDs can be used to estimate both ATT and CBF without significant discrepancies from the reference, which implies that the proposed H-CNN offers substantially reduced total scan time of multi-PLD PCASL.

Acknowledgements: This work was supported by NIH P30AG049638 and NIH RF1NS110043.

References: [1]Kim D, et al. *MRM*, 2023.

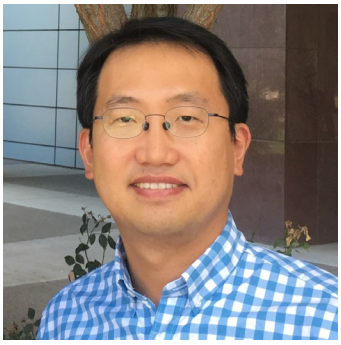

Reconstruction-free 3D imaging of positron-emitting radiotracers using ultrafast detectors and artificial neural network

[1]Sun Il Kwon, [2]Ryosuke Ota, [1]Daehee Lee, [1]Hamidreza Hemmati, [1]Eric Berg, [2]Norihiro Harada, [1,3]Simon R. Cherry

[1]Department of Biomedical Engineering, UC Davis
[2]Central Research Laboratory, Hamamatsu Photonics K.K., Hamamatsu, Japan
[3]Department of Radiology, UC Davis

Three-dimensional biomedical imaging techniques, including X-ray CT, SPECT, and PET, measure one- or two-dimensional projections from the object of interest. These projections are subsequently reconstructed into cross-sectional images or three-dimensional image volumes via analytic computed tomography algorithms. In all of these imaging modalities, a measured data point does not have a 1:1 correspondence with a point in image space, and the spatial distribution of the signal must be inferred by a reconstruction step. Accurate tomographic image reconstruction also depends on adequate angular sampling of the data. Uniquely for positron-emitting radiotracers used in PET, two annihilation gamma photons are emitted by the radiotracers in back-to-back directions. Therefore, ultimately, cross-sectional images or three-dimensional images of the radiotracers can be directly obtained by measuring the difference in arrival time of the two photons without any reconstruction step. The first reconstruction-free positron emission imaging was demonstrated by using two ultrahigh timing-resolution gamma-ray detectors and convolutional neural networks *(1)*. This imaging technique is referred to as direct positron emission imaging (dPEI). By removing the typical constraints associated with the sampling necessary for tomographic reconstruction, dPEI opens up many new possibilities for designing novel imaging systems. This presentation will focus on 1) the principle of dPEI, 2) the current progress and technology roadmap toward dPEI scanner systems, and 3) the new opportunities for the application of dPEI in biomedical research.

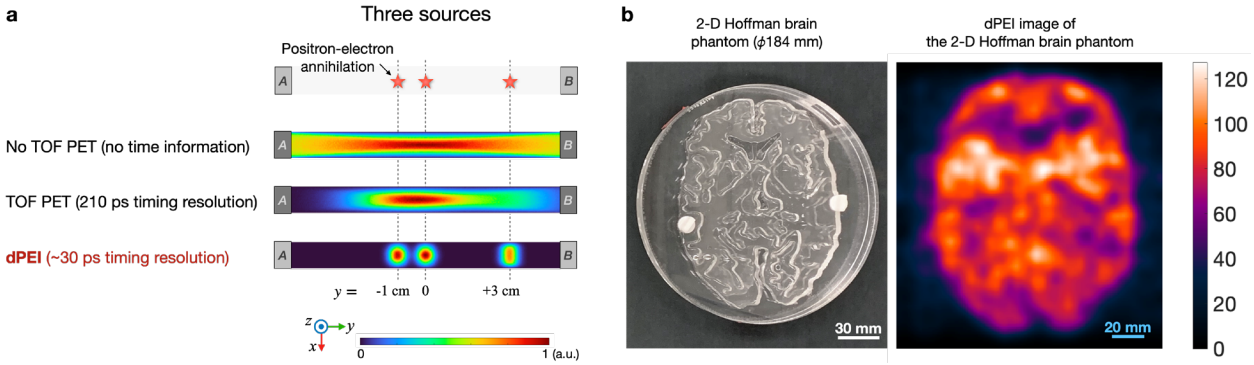

Figure 1. ***a,*** *Basis for direct positron emission imaging (dPEI).* ***b,*** *Cross-sectional dPEI image (right) of the 2-D Hoffman brain phantom (left) (1).*

Reference:

1. Kwon SI, Ota R, Berg E, Hashimoto F, Nakajima K, Ogawa I, Tamagawa Y, Omura T, Hasegawa T, Cherry SR. Ultrafast timing enables reconstruction-free positron emission imaging. *Nature Photonics*. 2021;15, 914–918.

Total Body versus Conventional PET/CT in Lymph Node Staging of Non-Small Cell Lung Cancer

Contributors: **R N Lee**, M H Madani, Y Mohammad, Y G Abdelhafez, B A Spencer, F Sen, D T Cooke, T Li, R D Badawi, L Nardo

Introduction: Compared to a conventional PET/CT, total body PET/CT has a 15-68 fold increase in sensitivity and improved spatial resolution. These features have the potential to improve the staging of lung cancer. This study evaluates total-body PET/CT (TBP) versus a conventional PET/CT (CP) in characterization of thoracic LN staging of patients with NSCLC using pathology as ground truth.

Methods: This is a prospective randomized two-arm single center trial in which 15 subjects presented for initial FDG PET/CT staging of NSCLC. Subjects were injected with 296-444 MBq of 18F-FDG and rested for 60 minutes. Subjects in arm 1 were scanned on a CP (Siemens mCT) followed by TBP (United Imaging uEXPLORER); subjects in arm 2 were scanned on TBP followed by CP. Each scan was 22 minutes. Biopsied LN stations were mapped to corresponding PET/CT scans. Two radiologists independently evaluated the probability of malignancy in the mapped LNs using a 5-point grading scale (1 = benign, 2 = likely benign, 3 = possibly malignant, 4 = likely malignant, and 5 = malignant).

Results: 58 thoracic lymph nodes were biopsied. 7/58 were malignant. Two false negative readings on the CP and none on the TBP were reported by both observers. Both observers also reported a false positive result on both TBP and CP. Sensitivity, specificity, PPV, NPV, and accuracy on TBP were 86% (42-100%), 98% (90-100%), 86% (46-98%), 98% (89-100%), and 97% (88-100%). For CP, the respective values were 71% (29-96%), 98% (90-100%), 83% (40-97%), 96% (89-99%), and 95% (85-99%).

Conclusion: The results suggest a potential for lymph node upstaging on TBP. This study also reaffirms the high sensitivity and accuracy of TBP in cancer staging. Given the small cohort size and low number of positive lymph nodes, further investigation is warranted. Limitations include difficulty in mapping biopsy-proven lymph nodes to PET/CT images.

Optimization of Total-Body PET Imaging of Bone Marrow Using Dual-Energy CT

Siqi Li[1], Benjamin A. Spencer[2,1], Yasser G. Abdelhafez[1,2] Yiran Wang[1,2], Heather Hunt[1], J. Anthony Seibert[1], Lorenzo Nardo[1], Simon R. Cherry[2,1], Ramsey D. Badawi[1,2], and Guobao Wang[1]

1. Department of Radiology, University of California – Davis
2. Department of Biomedical Engineering, University of California – Davis

Introduction: Bone marrow (BM) quantification with ^{18}F-FDG PET is of clinical significance for detecting BM involvement in cancer staging and early prediction of response to immunotherapy. However, current BM quantification may be inaccurate because a unit volume of bone marrow may also consist of spongy bone in which FDG activity is negligible, resulting in a potential underestimation of true BM uptake. Here we demonstrate this bone-led tissue fraction effect using DECT material decomposition and its impact on BM quantification.

Methods: Five cancer patients were scanned on the uEXPLORER total-body PET/CT scanner, and each dynamic dataset was acquired for 60 minutes. Prior IRB approval and informed consent were obtained. A DECT scan was performed with 80 kVp and 140 kVp to decompose each voxel into air, soft tissue and bone components. Kinetic modeling using a two-tissue compartmental model was performed for quantification over 80 bone ROIs (8/scan, on lumbar and thoracic vertebrae) with the ascending aorta as image-derived input function. A unit volume of bone marrow that can be measured with PET is a mix of true BM, cortical bone and blood. The total measured ^{18}F-FDG activity is a weighted sum of the activity of these three compositions, where the weight corresponds to the respective volume fraction. FDG uptake in cortical bone is negligible. The bone volume fraction from DECT was fixed in kinetic model estimation.

Results: A DECT image pair and corresponding fractional images are shown in Fig. 1A. With bone fraction correction (BFC), SUV was 1.8±0.33 compared to 1.6±0.31 without BFC. The FDG net influx rate K_i and delivery rate K_1 with BFC achieved 0.0063±0.0016 and 0.18±0.06 compared to 0.0057±0.0015 and 0.16±0.059 without BFC. Those changes were all statistically significant by paired t test (Fig. 1B).

Conclusion: Our study suggests current SUV and kinetic quantification of BM are likely underestimated in PET due to the significant bone volume fraction. A future work is to investigate the impact of this correction for BM quantification in blood cancer staging.

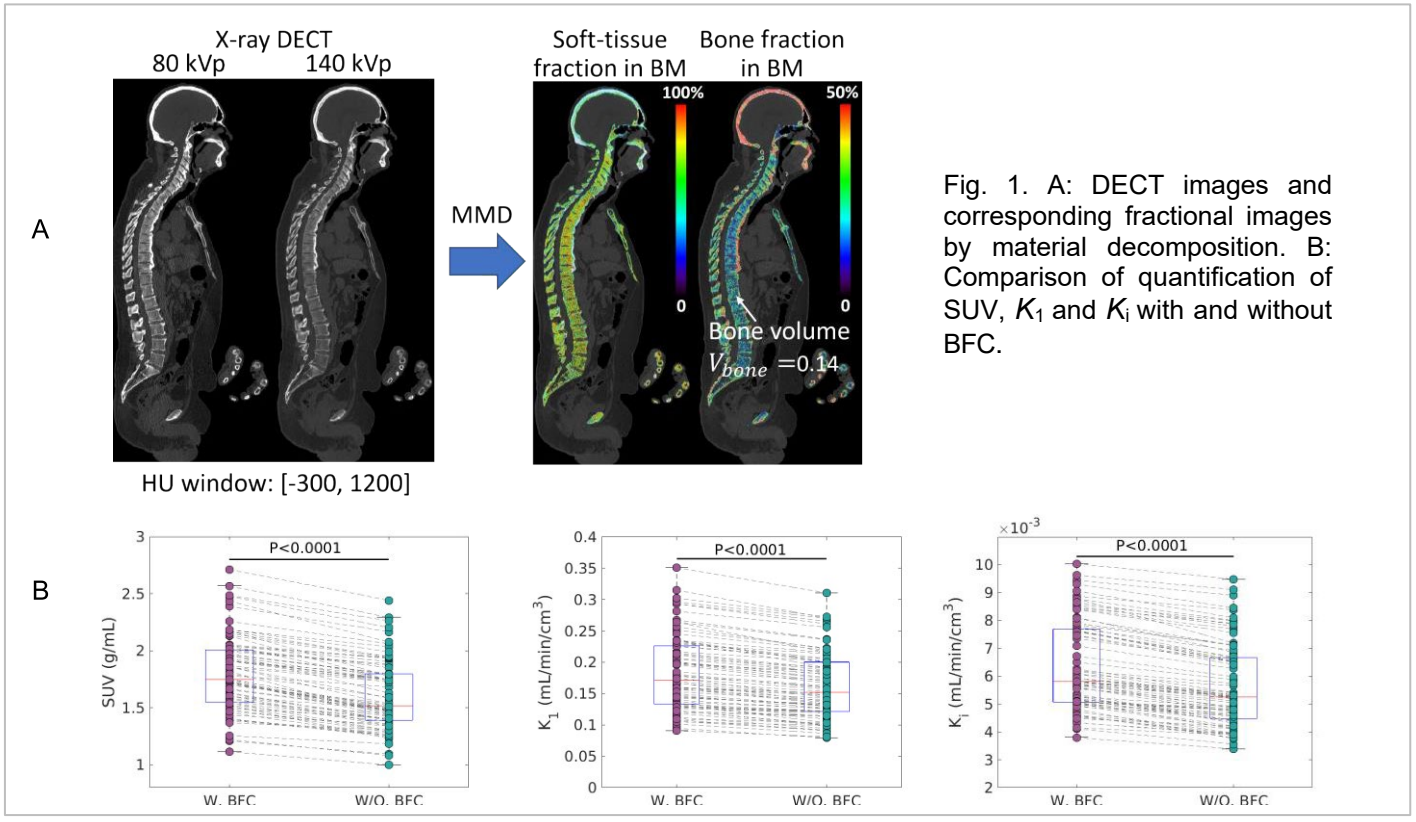

Fig. 1. A: DECT images and corresponding fractional images by material decomposition. B: Comparison of quantification of SUV, K_1 and K_i with and without BFC.

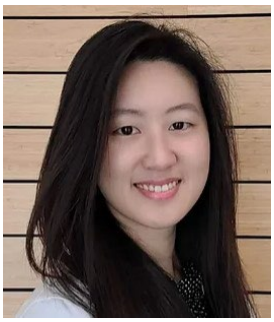

Long-term Percutaneous Cholecystostomy Treatment Course of Patients with Biliary Disease

Authors: **Katherine Liu, B.S.**; Michael Larson, M.D. Ph.D.

Background/Purpose: In patients presenting with acute cholecystitis, the gold standard treatment is cholecystectomy. For high-risk patients, percutaneous cholecystostomy (PC) may be offered as a bridge to definitive cholecystectomy, though some patients never become surgical candidates. Gallbladder thermoablation is an emerging, minimally-invasive technique that may be beneficial to patients who are not surgical candidates at the time of presentation. The study aim was to characterize patients who received PC at a tertiary academic hospital to evaluate the need for gallbladder thermoablation.

Methods: A retrospective chart review of image-guided PC patients from 2002-2016 to allow for >5 years of follow-up. 129 patients were identified as potential.

Results: At PC placement, average age was 58.67 years, American Society of Anesthesiology classification score (ASA) was 2.86, BMI was 28.5, and the most common comorbidities were hypertension, coronary disease, and diabetes.

41 patients had cholecystectomy an average 162 days after PC. 54 patients had PC tube removal, with an average tube dwell time of 95 days until removal. 21 patients died with a cholecystostomy tube in place an average 202 days (median 36) after PC. Of patients that died with PC in, Kaplan-Meier curve analysis showed no differences in survival when comparing male and female, old and young, and those presenting with or without co-morbid conditions.

Conclusions: Although patients receiving PC instead of cholecystectomy are thought to be elderly and frail, our study found a younger than expected average age of 58.67 years. PC is typically indicated at ASA scores 3-4, but most of our patients fell within ASA classes 2-3. This exploratory chart review confirms that there are patients who receive long term PC who could benefit from gallbladder thermoablation.

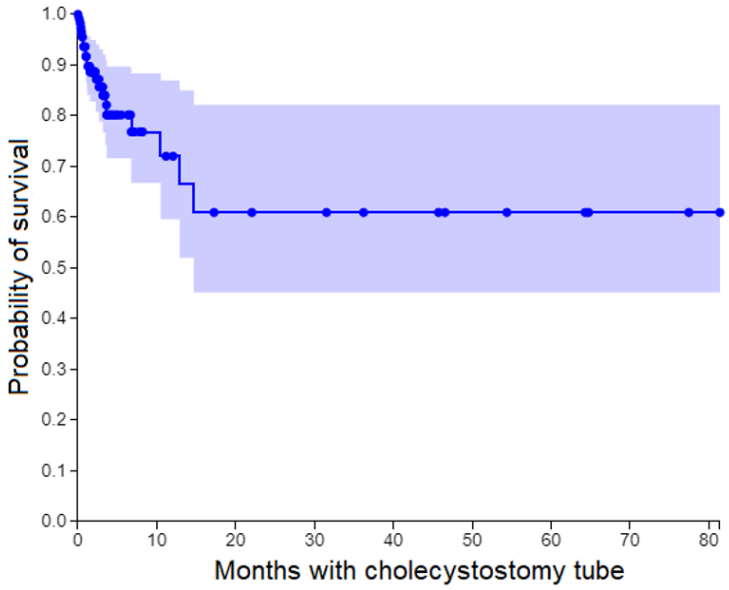

Total-body PET quantitative biomarkers reveal key differences in enthesitis between Rheumatoid and Psoriatic Arthritis

Dario F. Mazza[1], M.Sc., Yasser G. Abdelhafez[1,2], M.D., Ph.D., Siba P. Raychaudhuri[3], M.D., Abhijit J. Chaudhari, Ph.D.[1]

[1]Department of Radiology, University of California Davis
[2] Nuclear Medicine Unit, South Egypt Cancer Institute, Assiut University, Egypt.
[3] Department of Internal Medicine – Rheumatology, University of California Davis

Introduction: We sought to evaluate the ability of total-body PET (TB-PET) biomarkers to quantify enthesitis in Psoriatic (PsA) and Rheumatoid Arthritis (RA). We hypothesized that objective characterization of specific disease domains will allow PET to reliably distinguish between the two and add to current understanding of in-vivo pathology.

Methods: We present results of 39 patients (15 with RA, 24 with PsA). Participants underwent an ultra-low dose, single time-point TB-PET/CT scan using the [18F]FDG radiotracer. Thirty-eight entheses per participant were evaluated on PET, according to standard enthesitis measures.

Summed Likert grades (graded 0-3, across entheses) and summed SUVmax across entheses were used to compare between groups. Differences were assessed via Mann Whitney U-tests. Receiver operating characteristic (ROC) curves were used to test diagnostic potential.

Results: The total number of PET-positive entheses was higher in participants with PsA (8.83 ± 5.1) compared to RA (4.25 ± 2.7, $p < 0.05$). Across all the 38 entheses sites, there was a significant difference in both summed Likert grades and summed SUVmax between groups ($p < 0.01$, Figure 1). There were significant differences for the MASES and SCPARCC entheses subsets ($p<0.05$), but not for the LEI subset. ROC analysis showed that both summed scores can perform acceptably as binary classifiers. The AUC values were 0.76 (95% CI 0.63-0.90) and 0.79 (95% CI 0.63-0.91) (summed scores and summed SUV Max, respectively) for the San Francisco subset, followed by (0.76, 0.78), and (0.71, 0.72) for the MASES and SPARCC. These scores performed less well on the 4-point (0.69, 0.69) and LEI (0.56, 0.58) subsets.

Conclusion: Our results demonstrate that PET measures can be used to quantify disease domains in autoimmune arthritis, and potentially distinguish between these two conditions. Differing performance of site groupings calls for further validation against standard clinical evaluations and other imaging modalities.

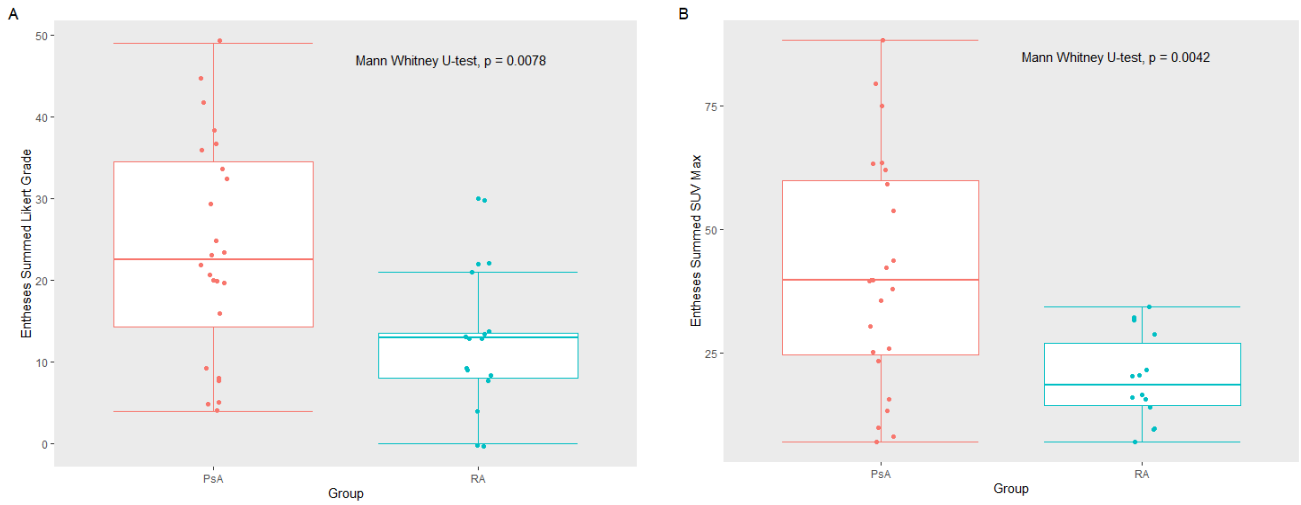

Figure 1: (A) Summed Likert grading of active entheses sites for PsA and RA participants; (B) Summed SUV max of active sites in PsA and RA participants.

Financial Disclosure: UC Davis receives institutional research support from United Imaging Healthcare, the manufacturer of the EXPLORER PET/CT scanner. However, none of the authors receive direct support from United Imaging Healthcare, and no other potential conflicts of interest relevant to this article's authorship exist.

Funding: National Psoriasis Foundation and National Institutes of Health (grants R01 AR076088 and R01 CA206187).

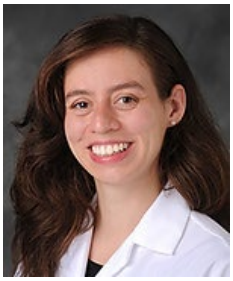

Non-contrast Head CT Protocol Development & Optimization on a High-Resolution CT Platform

Sarah McKenney, Ph.D., Kader Karli Oguz, M.D., Nazanin Azizi, M.D., Jennifer Chang, M.D., Lotfi Hacein-Bey, M.D., Arzu Ozturk, M.D.

Introduction: An ultra-high-resolution CT (HRCT) platform was acquired by UC Davis in April 2019. Subsequently, a continuous image quality optimization process was undertaken on non-contrast head protocols, focused on contrast-to-noise ratio (CNR) and image noise.

Methods: Iterative evaluation and optimization of image quality and radiation dose on the Canon Aquilion Precision platform, with a standard 512 matrix reconstruction/0.5 mm slice thickness, and 1024/2048 matrices with a minimum slice thickness of 0.25 mm.
Intervention points:

1. Late 2020, system update with deep learning noise reduction reconstruction scheme (AiCE).
2. Move from 1024 to 512 matrix to accommodate limitations in retrieving and displaying large imaging datasets. Matrix reduction and larger focal spot size resulted in image noise reduction.
3. Reconstruction kernel adjustment to improve noise texture.

Results: Head CT protocols on HRCT were refined via iterative interventions. Ultimately, optimization resulted in a CTDI vol of 60.4 mGy, (13% more than average CTDIvol from initial installation, but well below ACR reference level of 75 mGy). Protocol optimization of head CTs resulted in significant contrast enhancement between WM and GM, improved diagnostic quality, and positive clinical impact on emergency indications, i.e. stroke.

Conclusion: High resolution capability CT scanners such as photon counting systems are increasingly being used. CT is a critical imaging tool in neurological emergencies, being widely available, fast, and with high spatial resolution. Intracranial hemorrhage and acute stroke are core neurological emergencies that rely heavily on CT. CT is mainly limited by contrast resolution, especially non-enhanced CT (NECT). HRCT quality improvement strategies include larger matrix sizes, as diagnostic value is based on detecting subtle changes in tissue attenuation between gray matter (GM) and white matter (WM) which have clinical significance, particularly in acute stroke. Optimization of Canon head CTs caused slightly increased radiation accompanied by reduced image noise and, therefore, higher contrast-to-noise ratio (CNR).

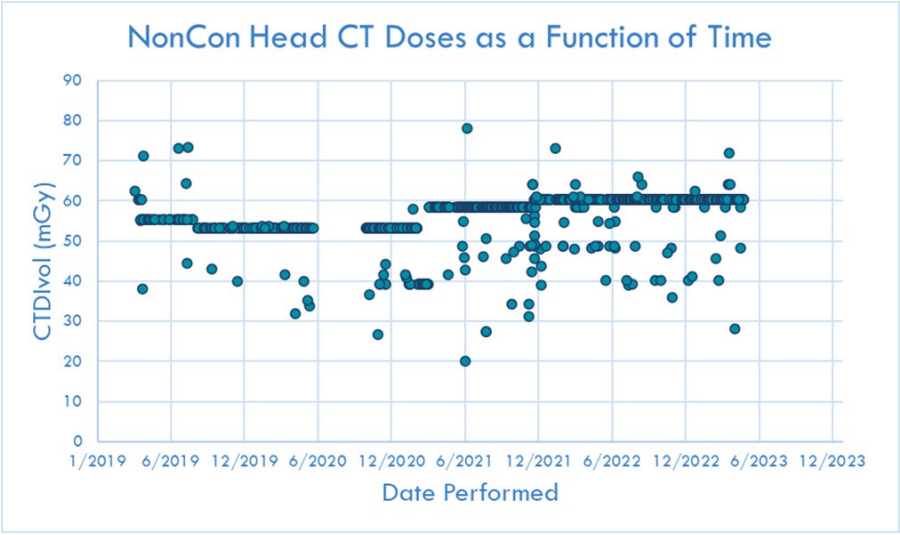

References

1.Diaconis JN, Rao KC (1980) CT in head trauma: a review. J Comput Tomogr 4:261–270 2.
2.Kloska SP, Nabavi DG, Gaus C, Nam EM, Klotz E, Ringelstein EB, Heindel W (2004) Acute stroke assessment with CT: do we need multimodal evaluation? Radiology 233:79–86
3.Craddock C, Chen MY, Dixon RL, Schlarb CA, Williams DW 3rd (2006) The effect of skull volume and density on differentiating gray and white matter on routine computed tomography scans of the head. J Comput Assist Tomogr 30:734–738 7.
4.Love A, Siemund R, Hoglund P, Van Westen D, Stenberg L, Petersen C, Bjorkman-Burtscher IM (2014) Hybrid iterative reconstruction algorithm in brain CT: a radiation dose reduction and image quality assessment study. Acta Radiol 55:208–217 8.
5.Korn A, Fenchel M, Bender B, Danz S, Hauser TK, Ketelsen D, Flohr T, Claussen CD, Heuschmid M, Ernemann U, Brodoefel H (2012) Iterative reconstruction in head CT: image

Sonographic Assessment of Acute Versus Chronic Cholecystitis: An Ultrasound Probability Stratification Model

Navarro SM, Chen S, Situ X, Corwin MT, Loehfelm T, Fananapazir G.

Introduction: The distinction between acute and chronic cholecystitis is challenging by ultrasound (US). Most studies compare the US features of acute cholecystitis vs. no acute cholecystitis and do not consider chronic cholecystitis. Therefore, we sought to investigate which sonographic variables most contributed to the diagnosis of acute versus chronic cholecystitis.

Methods: The surgical pathology database was reviewed to identify adult patients who underwent cholecystectomy for cholecystitis and had a preceding ultrasound of the right upper quadrant within 7 days. A total of 236 patients were included in the study. A comprehensive imaging review was performed to assess for gallstones, gallbladder wall thickening, gallbladder distension, pericholecystic fluid, gallstone mobility, the sonographic Murphy's sign, mural hyperemia, and the common hepatic artery peak systolic velocity.

Results: Of 236 patients with a cholecystectomy, 119 had acute cholecystitis and 117 had chronic cholecystitis on surgical pathology. Statistical models were created for prediction. The simple model consists of three sonographic variables and has a sensitivity of 60% and specificity of 83% in predicting acute versus chronic cholecystitis. The most predictive variables for acute cholecystitis were elevated common hepatic artery peak systolic velocity, gallbladder distension, and gallbladder mural abnormalities. If a patient had all three of these findings on their preoperative ultrasound, the patient had a 96% chance of having acute cholecystitis. Two of these variables gave a 73-93% chance of having acute cholecystitis. One of the three variables gave a 40-76% chance of having acute cholecystitis. If the patient had 0 of 3 of the predictor variables, there was a 29% chance of having acute cholecystitis.

Conclusions: Gallbladder distension, gallbladder mural abnormalities, and elevated common hepatic artery peak systolic velocity are the most important sonographic variables in predicting acute versus chronic cholecystitis.

Table 1. Univariate Analysis of All Variables

Variable	All Patients (n = 236), Mean (±SD) or n (%)	Acute (n = 119), Mean (±SD) or n (%)	Chronic (n = 117), Mean (±SD) or n (%)	*P*-Value
Gallbladder wall thickness (in mm, n = 235)	3.3 ± 1.9	3.9 ± 2.2	2.8 ± 1.4	<.001
HAV (in cm/second, n = 199)	98.9 ± 46.6	103.9 ± 49.6	93.8 ± 42.9	.109
Age (in year, n = 236)	46.2 ± 17.3	49.3 ± 17.0	43.1 ± 17.0	.004
Cholelithiasis				.568
Yes	224 (94.9)	114 (95.8)	110 (94.0)	
No	12 (5.1)	5 (4.2)	7 (6.0)	
GS in neck				.641
Yes	162 (68.9)	83 (70.3)	79 (67.5)	
No	73 (31.1)	35 (29.7)	38 (32.5)	
Immobile GS				.708
Yes	100 (42.4)	49 (41.2)	51 (43.6)	
No	136 (57.6)	70 (58.8)	66 (56.4)	
Murphy's sign				.022
Yes	92 (39.0)	55 (46.2)	37 (31.6)	
No	144 (61.0)	64 (53.8)	80 (68.4)	
Peri-GB fluid				.001
Yes	36 (15.3)	27 (22.9)	9 (7.7)	
No	199 (84.7)	91 (77.1)	108 (92.3)	
GB distension				<.001
Yes	55 (23.3)	41 (34.5)	14 (12.0)	
No	181 (76.7)	78 (65.6)	103 (88.0)	
Wall abnormality				<.001
Yes	54 (22.9)	45 (37.8)	9 (7.7)	
No	182 (77.1)	74 (62.2)	108 (92.3)	
Mural hyperemia				.005
Yes	26 (11.2)	20 (17.0)	6 (5.2)	
No	207 (88.8)	98 (83.1)	109 (94.8)	
Gender				<.001
Male	70 (29.7)	48 (40.3)	22 (18.8)	
Female	166 (70.3)	71 (59.7)	95 (81.2)	

Variables were compared between acute versus chronic cholecystitis using Wilcoxon rank-sum tests for continuous variables or χ^2 tests (or Fisher exact tests when count ≤5) for categorical variables.

Dynamic Imaging of ^{18}F-AraG in Healthy Individuals and a Non-small Cell Lung Cancer Patient Undergoing Anti-PD-1 Immunotherapy

Negar Omidvari[1*], Jelena Levi[2], Yasser G Abdelhafez[3,4], Yiran Wang[1,3], Lorenzo Nardo[3], Megan E Daly[5], Guobao Wang[3], and Simon R Cherry[1,3]

[1] Department of Biomedical Engineering, UC Davis, Davis, CA, USA. [2] CellSight Technologies Inc., San Francisco, CA, USA. [3] Department of Radiology, UC Davis Medical Center, Sacramento, CA, USA. [4] Radiotherapy and Nuclear Medicine Department, South Egypt Cancer Institute, Assiut University, Egypt. [5] Department of Radiation Oncology, UC Davis Comprehensive Cancer Center School of Medicine, Sacramento, CA, USA. *Email: nomidvari@ucdavis.edu

Introduction: Immunotherapies, especially checkpoint inhibitors like anti-PD-1 antibodies, have transformed cancer treatment by leveraging the patient's immune system to target and kill cancer cells. However, predicting immunotherapy response remains challenging. Molecular imaging techniques using novel radiotracers such as ^{18}F-AraG could offer non-invasive quantification of total-body immune cell activity, aiding in identifying potential responders. The aim of this study was to obtain preliminary data on pharmacokinetics of ^{18}F-AraG, as a potential quantitative biomarker for immune response evaluation.

Methods: The study consisted of 90-min total-body dynamic scans of four healthy subjects and a non-small cell lung cancer (NSCLC) patient, scanned before and after anti-PD-1 immunotherapy. Compartmental modeling with Akaike information criterion model selection was employed to analyze tracer kinetics in various organs, including seven regions of a NSCLC tumor and four tumor-draining mediastinal lymph nodes. Practical identifiability analysis was performed to assess reliability of kinetic parameter estimation. Correlations of SUV, SUVR (tissue-to-blood ratio), and Logan plot slope (K_{Logan}) with total volume-of-distribution (V_T) were calculated to identify potential surrogates for kinetic modeling.

Results: The study showed that although ^{18}F-AraG SUV images can serve for baseline tumor classification, but kinetic modeling or graphical analysis methods may be required for accurate quantification of immune response changes post-therapy. While SUV changes varied in different regions of the tumor post-therapy, the SUVR, K_{Logan}, and V_T showed increasing trends in all regions of the tumor with high identifiability. Strong correlations were observed between K_{Logan} and SUVR values with V_T, suggesting them as promising surrogates for V_T.

Conclusion: Our findings highlight the promising role of ^{18}F-AraG dynamic imaging as a non-invasive biomarker for quantifying the immune response to therapeutic interventions in cancer patients. The promising total-body kinetic modeling results also suggest potentially wider applications of the tracer in investigating the role of T cells in the immunopathogenesis of diseases.

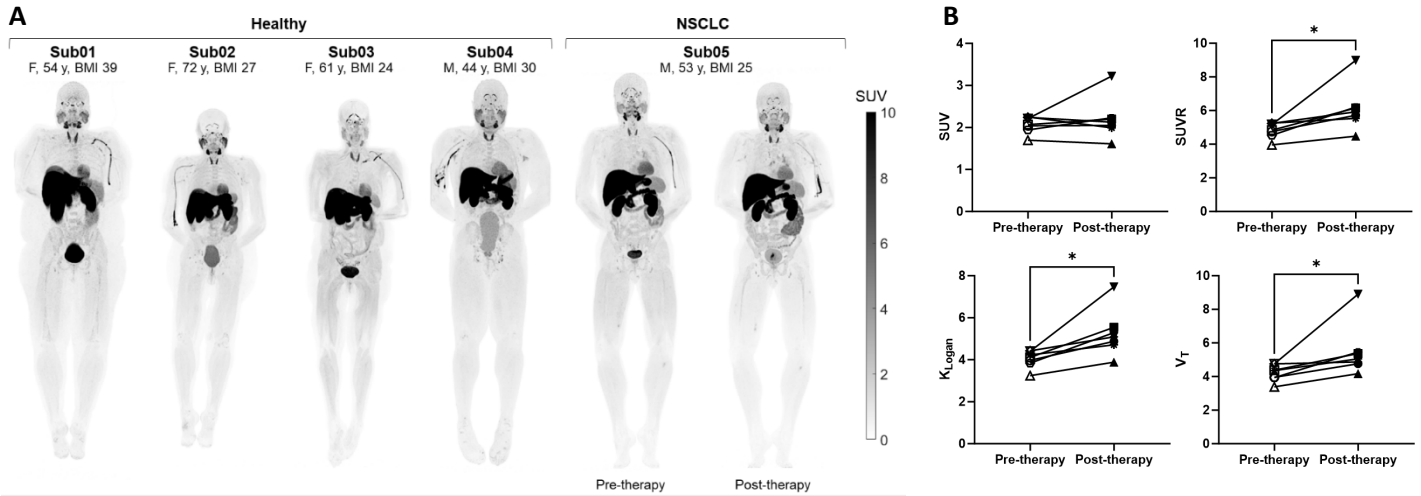

Figure 1. (A) Maximum intensity projections of SUV images (50–60 min p.i.) of the four healthy control subjects and one NSCLC patient scanned before and after immunotherapy. (B) Changes of SUVmean, SUVR, K_{Logan}, and V_T in different regions of the NSCLC tumor after immunotherapy.

Automated skull stripping of MRI brain scans of mice exposed to a chemical threat agent using 2D U-Net

V. A. Porter[1,2], B. A. Hobson[1,3], B. Foster[4], P. J. Lein[5], and A. J. Chaudhari[2,3]

[1]Biomedical Engineering; [2]Radiology; [3]Center for Molecular and Genomic Imaging; [4]TechMah Medical LLC; [5]Molecular Biosciences; University of California, Davis

Introduction: Tetramethylenedisulfotetramine (TETS) is a rodenticide that triggers seizures and *status epilepticus (SE)* in humans. There is great interest in utilizing *in vivo* imaging methods in mouse models of TETS-induced *SE* to study resulting neuropathology and assess novel neuroprotective treatments. Recently, we developed a 2D U-Net-based framework for whole brain delineation (WBD) of MRI brain scans of rats exposed to an organophosphate. In this work, we tested the hypothesis that the pre-trained U-Net framework is generalizable to other pathologies and can perform automated WBD of T_2-weighted MRI scans in a mouse model of TETS exposure.

Methods: The convolutional neural network had a modified 2D U-Net architecture and was pre-trained with 100 rat brain T_2-weighted MRI scans. Our data consisted of T_2-weighted MRI mouse brain scans (n=50, 35 slices/scan, voxel size: 125x125x250μm, matrix size: 160x160x35, acquired on a Bruker BioSpec 7T scanner, phased array coil) and matching manual whole brain segmentations. Scans were of C57BL/6J mice from a TETS study that compared neuroprotective therapies (midazolam (MDZ), allopregnanolone (ALO), MDZ and ALO combination (DUO)) to vehicle controls (VEH) at three timepoints (3-, 7-, and 28-days post-TETS exposure). MRI scans were preprocessed by applying N4ITK bias correction and down-sampling the resolution of each slice ([160x160x35] to [128x128x35]). To evaluate pre-trained U-Net performance, dice coefficients (DC) and Hausdorff distances (HD) were calculated between U-Net-generated labels and manual segmentations.

Results and Conclusion: The U-Net-generated labels achieved a DC and HD (median[range]) of 0.98[0.95-0.99] and 1.16[0.99-2.39]mm, respectively, demonstrating outstanding accuracy that was comparable to rat scan outcomes. Segmentation time was 6 seconds/scan. We conclude that the pre-trained 2D U-Net-based framework provided a fully automated, efficient, and accurate segmentation approach, without additional training. Future research will include evaluating U-Net-framework in image analysis pipelines, and examining the applicability in other preclinical animal models.

A

Table 1: Mouse WBD Accuracy (DC) of 2D U-Net

Group	# of Scans	Median	Range
MDZ	18	0.9830	0.9529-0.9881
ALO	11	0.9807	0.9713-0.9867
DUO	15	0.9812	0.9546-0.9851
VEH	6	0.9820	0.9821-0.9831
Timepoint	**# of Scans**	**Median**	**Range**
Day 03	17	0.9825	0.9710-0.9881
Day 07	17	0.9820	0.9546-0.9861
Day 28	16	0.9821	0.9529-0.9848

B

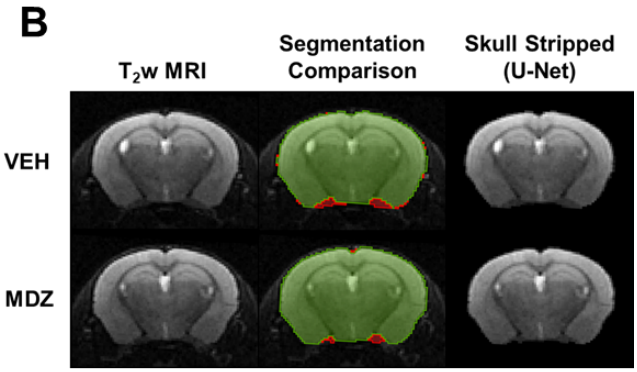

Figure 1: A) 2D U-Net segmentation results; (top to bottom): VEH, and TETS-exposed mouse from the MDZ treatment group. Columns from left to right: anatomical MRI, segmentations from 2D U-Net (green: correctly labeled pixels, red: incorrectly labeled pixels), and skull-stripped MRI using the U-Net label.

Important role of ultrasound in assessing tubulocystic renal cell carcinoma

Ethan Radzinsky, Tara Morgan, Shannon Navarro, Nirvi Dahiya, Maitray Patel, Ghaneh Fananapazir

Purpose: To assess the imaging features of tubulocystic renal cell carcinoma, a new pathologic entity.

Methods: This retrospective, single institution study involved searching the pathology database between 2016 and 2023 for cases of tubulocystic subtype of renal cell carcinoma. Relevant demographic and clinical data were collected, and multimodality imaging features were described.

Results: The study population comprised seven patients (6 male, 1 female; mean age, 61 ± 7 [SD] years) with pathology-proven tubulocystic renal cell carcinoma. Clinical features included 2 patients with abdominal pain and one patient with hematuria. The remaining three cases were discovered incidentally on imaging and one was discovered on surveillance for known testicular cancer. Six of the seven cases exhibited a round morphology, while the remaining case was bilobed. The mean maximal tumor diameter was 2.4 cm (range 1.4 – 4.8 cm). CT imaging showed mean unenhanced contrast attenuation of 15.3 Hounsfield Units (HU) (range 5.6 - 37.2) and a contrast-enhanced mean of 22.6 HU (range 5 - 42.3). Ultrasound was performed on five patients, revealing a variety of findings: three patients exhibited a uniformly hyperechoic mass, one showed a hyperechoic mass with central hypoechogenicity, and one showed a hypoechoic septated cyst. Notably, all the lesions demonstrated posterior acoustic enhancement. The patient with a septated cystic appearance underwent contrast-enhanced ultrasound, which demonstrated septal enhancement. Contrast-enhanced MRI was performed on five patients. All lesions were T1 hypointense and T2 hyperintense, with a single exception showing mixed T2 signal intensity. MRI enhancement was noted in three cases, characterized by either enhancing septa (2/5) or an enhancing mural nodule (1/5). Two of the four hyperechoic masses on ultrasound displayed enhancement on MRI; enhancement was seen in the hyperechoic portion of the mixed echogenic mass.

Conclusions: The imaging features of tubulocystic renal cell carcinoma on CT and MRI and can be mistaken for cysts. However, ultrasound in most cases shows an echogenic lesion with posterior acoustic enhancement. Ultrasound may, therefore, provide crucial additional information in instances where CT imaging findings are ambiguous or inconclusive.

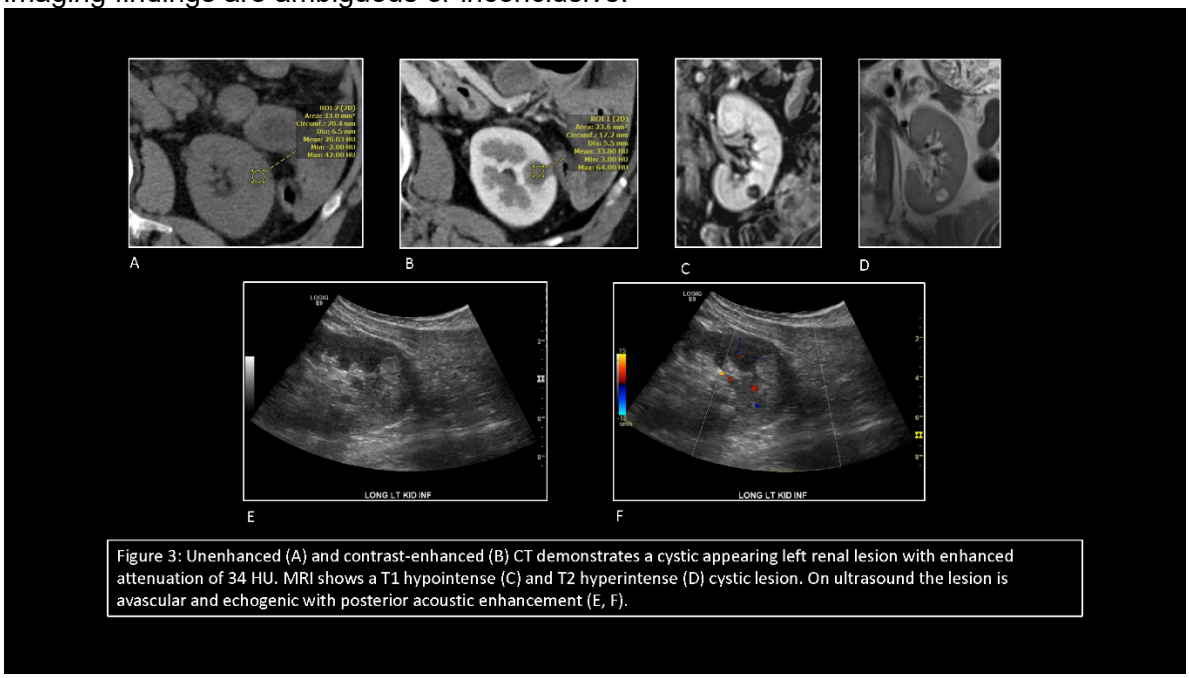

Figure 3: Unenhanced (A) and contrast-enhanced (B) CT demonstrates a cystic appearing left renal lesion with enhanced attenuation of 34 HU. MRI shows a T1 hypointense (C) and T2 hyperintense (D) cystic lesion. On ultrasound the lesion is avascular and echogenic with posterior acoustic enhancement (E, F).

Practicality of Capturing PET Detector Signals Using TDC Timing Information

A. Refaey[1], Ramsey D. Badawi[1,2]

[1]Department of Biomedical Engineering, University of California, Davis
[2]Department of Radiology, University of California, Davis

Introduction: In this study, we propose a FPGA-based TDC for capturing the waveform of energy signals generated by PET detector. The TDC design offers high flexibility in measurement capabilities, enabling the recording of digital signals produced by the PET detector with a precision of 23 picoseconds. The TDC is implemented on a low-cost AMD Artix7 FPGA chip. The timing circuit generates the fine timing information by utilizing a Tapped-Delay Line (TDL) chain to monitor the leading edge of the energy signal that falls between two clock edges, and generates the energy information by adding the coarse counts to the fine counts. This approach provides an economic and high-resolution method for determining the temporal properties of signals produced by a PET detector.

Method: The PET detector is composed of a 3x3x20mm^3 LYSO scintillation crystal coupled to 3x3mm^2 SiPM via optical grease. The output pulse is fed into FPGA-based sigma-delta circuit where the change in the analog input is tracked by converting the difference in the LVDS inputs levels into a binary number, the value of that number is directly proportional to the detector integrated signal. TDL is composed of a series of 120 Xilinx fast carry logics. The waveform of signal is captured by taking snapshots as it propagates down the TDL. The Na-22 source is placed in the middle of two identical crystals (start and stop detectors) separated by a distance of 6 cm, and a total of 10,000 events were acquired. The data have not been corrected for the natural radioactivity arising from the lutetium in the scintillator material. The energy response in the TDL_{start} detector is captured and histogrammed, while the TDL_{start} and TDL_{stop} are used to produce the CTR data, as shown in figure 1. Concurrently, based on ToT method, a coarse counter tracks the duration that the start signal stays above a set threshold value. The coarse counter and TDC demonstrated energy resolution of 17.6% and 19.3% at the 511KeV photopeak, respectively. By subtracting the timing information obtained from TDL_{stop} and TDL_{start}, which was restricted by a timing window, a CTR of 202.1ps was obtained.

Conclusion: In conclusion, our digital TDC design utilizing a TDL chain has demonstrated efficacy in estimating both energy and timing with appropriate precision for PET applications. While this approach does come with a cost in terms of digital resources, it represents a promising solution for economic recording of PET detector signals.

References
[1] A. Refaey, G. Burkett, J. Du, R. D. Badawi, A Cost-Effective Field-Programmable-Gate-Array-based Pulse Processor for Biomedical Imaging Applications, 2020 IEEE NSS-MIC (virtual).
[2] Zhao et al., An Advanced 100-Channel Readout System for Nuclear Imaging. IEEE TIM, 68(9), pp. 3200-3210, Sep. 2019.

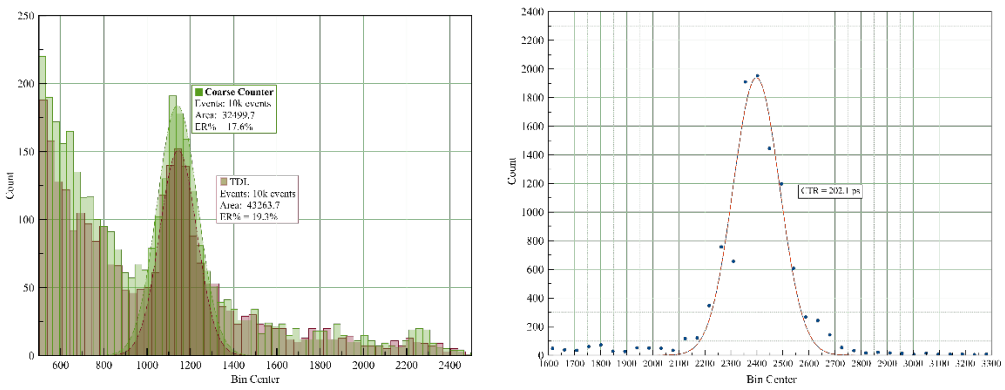

Fig. 1. Energy (left) and CTR (right) histograms

Characteristics of catheter injection for predictive particle transport modeling in Y-90 transarterial radioembolization procedures

Carlos A. Ruvalcaba[1], Avinash Rajamani[1], Emilie Roncali [1,2]

[1] Department of Biomedical Engineering, UC Davis
[2] Department of Radiology, UC Davis

Hepatic cellular carcinoma is one of the most common forms of liver cancer. Depending on the cancer's progression, treatment can include a combination of external radiation therapy, chemotherapy, or surgery. Radioembolization using microspheres loaded with a radioactive isotope such as yttrium-90 (Y-90) has shown promise increasing patient outcomes but requires personalized and complex planning due to sensitivity of liver tissue to radiation and the need to reach a certain threshold of radiation dose in the tumors. Our modeling framework, CFDose, incorporates clinical patient cone-beam Computed Tomography images to predict microsphere transport in the patient liver vasculature using computational fluid dynamics (CFD). For this work, we consider a finite-thickness catheter wall at injection points that are at least one generation downstream of either the left or right hepatic arteries (considered a super selective injection). These considerations are important when super selective injections are used since the catheter obstructs the vessel lumen significantly. We also consider the effects of the local injection curvature on the injection profile by considering increasing levels of tortuosity. The model geometry we employ is an idealized structure where the surface mesh is truncated following two bifurcations from the right hepatic arteries. Preliminary results indicate increased particle asymmetries downstream of a tortuous injection segment when compared to an idealized extrusion or considering only an idealized parabolic flow profile. The injection location geometries are motivated by a particular patient case where the microsphere injection occurred directly downstream of a curved vascular segment, requiring a second injection further downstream the hepatic arterial tree. In such cases, we recommend carefully considering the segment tortuosity on modeling Y-90 injection.

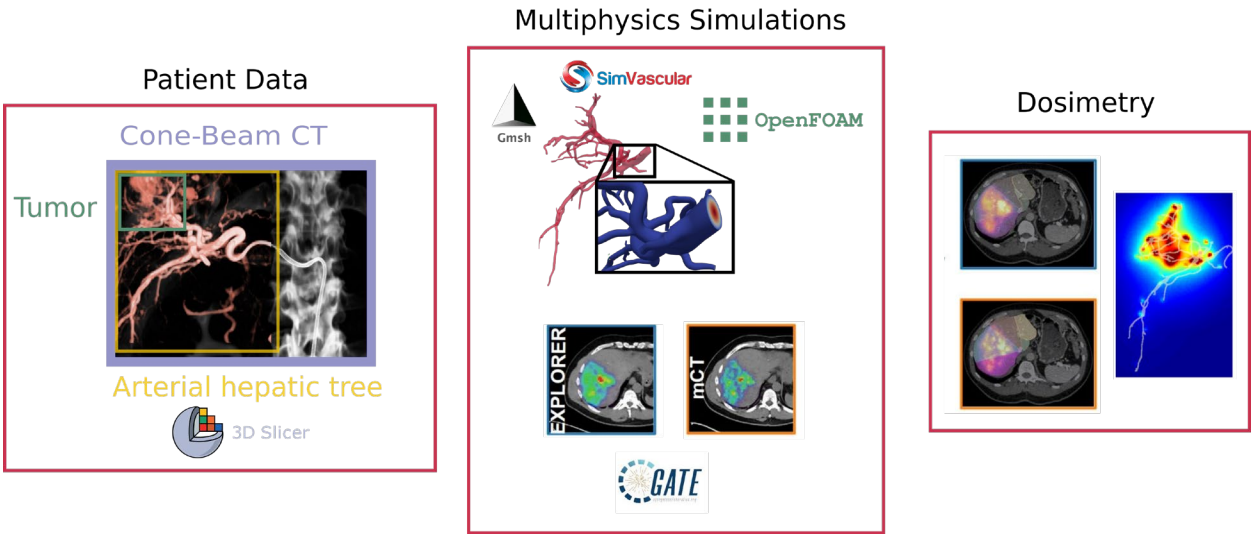

Figure 1: Overview of the workflow for CFDose, beginning with patient data and ending with personalized dosimetry. In the left-most panel, patient cone-beam CT data is processed to extract the arterial tree. The canter panel gives an overview of the tools used to combine CFD and Monte-Carlo simulations. Finally, in the right-most panel, the results are combined to give patient-specific dosimetry.

Activity painting phantom for positron emission tomography

Ekaterina Shanina[1], Benjamin Spencer[1,2], Tiantian Li[1,3], Reimund Bayerlein[2], George Burkett[2], Jinyi Qi[1], Simon Cherry[1,2]

[1]Department of Biomedical Engineering,
[2]Department of Radiology, University of California, Davis, Davis, CA
[3]United Imaging Healthcare Americas, Houston, TX

Introduction: The traditional positron emission tomography (PET) phantoms have a number of limitations, including fixed geometry, difficulty in changing contrast or introducing small changes within a single study. We propose a novel PET phantom design that overcomes many of these limitations and builds upon an earlier approach [1]. By collecting a single high-count event pool and sampling it to select only the needed number of counts for analysis, we can generate a variety of phantoms efficiently to test an imaging system both quantitatively and qualitatively.

Methods: To collect the event pool, we moved a ^{22}Na point source in the field of view (FOV) of the uEXPLORER total-body PET/CT scanner using a high-precision robotic arm. In this early study, the source traversed a single plane in the center of the FOV, moving at a constant speed one line at a time. To determine the source position, we divided the data set into short frames and reconstructed each frame. The source position was defined as the centroid of the activity distribution in each reconstructed frame. Finally, to demonstrate the flexibility in creating different phantom shapes, we defined multiple patterns, sampled the data pool, and reconstructed the resulting phantom images.

Results and discussion: A slice of the Belzunce brain phantom [2] representing the ^{18}F-FDG uptake and a slice of the 3D Hoffman brain phantom [3] representing an amyloid-negative scan with ^{18}F-flortaucipir are shown in figure 1. Overall, there is good agreement between target and reconstructed images.
Conclusions: In this study, we developed a proof-of-concept framework for a universal PET phantom that overcomes many limitations of the traditional phantoms. We acquired one large data pool and sampled it to produce multiple desired activity distributions that inherently contain the scanner parameters that are difficult to model computationally or theoretically.

References:

[1] Forgacs, Attila, et al., *Plos one* 14.1 (2019): e0207658
[2] Belzunce, Martin A., et al., *Medical Physics* 47.8 (2020)
[3] Harrison, Robert L., et al., *Medical Physics* 47.3 (2020)

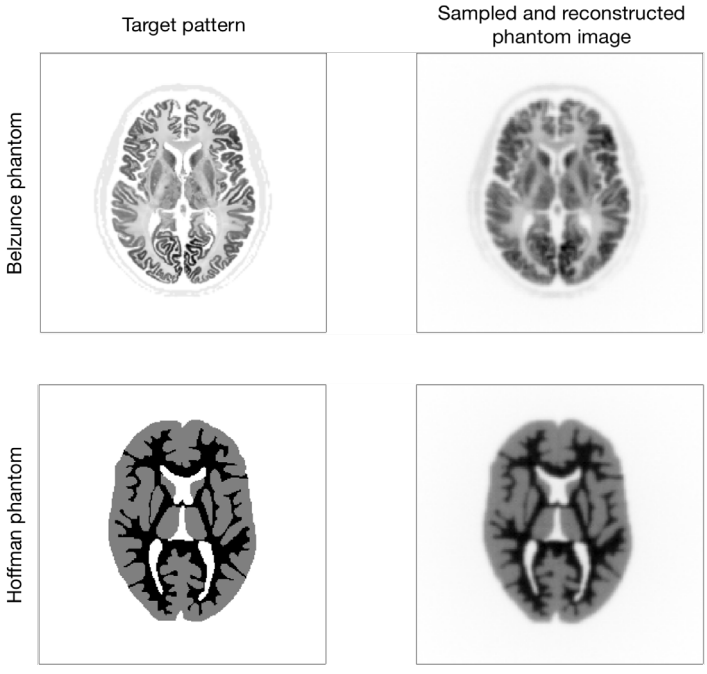

Figure 1: *Top row*: single slice of the Belzunce brain phantom representing ^{18}F-FDG uptake in a healthy brain. *Bottom row*: single slice of the 3D Hoffman brain phantom representing an amyloid-negative scan with ^{18}F-flortaucipir (grey:white = 1:2). *Left*: target patterns. *Right*: sampled and reconstructed phantom images. This figure illustrates how a single high-count dataset can be subsampled to produce arbitrary desired activity distributions.

Development of In-house Stringent Protocols and Phantoms for Quality Assurance of a Clinical and Research Total-Body PET Scanner

Benjamin A. Spencer[1,2], Negar Omidvari[2], Eric Berg[2], Enette M. Revilla[2], Reimund Bayerlein[1], Yasser G. Abdelhafez[1], George Burkett[1], Jeffrey P. Schmall[1,3], Mike Nguyen[1], Zhaoheng Xie[2], Elizabeth Li[2], Edwin K. Leung[1,2,3], Aaron Selfridge[2], Yansong Zhu[1], Yiran Wang[1,2], Heather Hunt[1], Kristin McBride[1], Lynda Painting[1], Ofilio Vigil[1], Denise T. Caudle[1], Guobao Wang[1,2], Emilie Roncali[1,2], Terry Jones[1], Lorenzo Nardo[1], Simon R. Cherry[2,1], Ramsey D. Badawi[1,2]

[1]Department of Radiology, and [2]Department of Biomedical Engineering, University of California Davis, CA, USA,[3]UIH America Inc., Houston, TX, USA

Background

With their widespread adoption in routine clinical care and a variety of research applications, total-body PET scanners will play a key role in the future of PET research. This work presents the methodology for a stringent and robust quality assurance program implemented on the world's first total-body PET scanner at UC Davis [1], including results from phantom and clinical quality assurance methods spanning three years of implementation.

Methods & Results

A. Daily count-rate monitoring: Average LYSO background singles-rate provides a fast and efficient daily check of the system performance (Figure 1A).

B. Quantitative accuracy: Weekly scans of a ^{68}Ge uniform cylinder in three axial locations can ensure quantitative accuracy is consistent axially and temporally [2] (Figure 1B).

C. Cross-calibration: Semi-annual scans of a uniform ^{18}F-filled phantom will ensure the scanner is accurately cross-calibrated with the dose calibrator (Figure 1C). This should be done following calibrations or more frequently if needed.

D. Image quality investigation: A quantitative investigation of the entire axial field-of-view (AFOV) is performed annually, using multiple NEMA image quality phantoms spanning the AFOV scanned at several activity levels representative of clinical and research protocols in use (following [3]).

E. Long-term temporal monitoring of system-wide performance with real patient data: Total-body scanners uniquely allow utilizing every human subject scan for quality assurance by calculating the ratio of the total human count-rate obtained from each subject scan to the known activity at scan time as an estimate of the temporal stability of the scanner (Figure 1D).

Conclusions

These quality assurance protocols ensure thorough and stringent examination of total-body PET scanner performance and stability to facilitate clinical care and research reliability.

References

1. Spencer BA, Berg E, Schmall JP, et al. Performance evaluation of the uEXPLORER Total-body PET/CT scanner based on NEMA NU 2-2018 with additional tests to characterize long axial field-of-view PET scanners. *J Nucl Med.*, 2021;62:861–870.
2. Nguyen M, McBride K, Hunt H, et al. Temporal and Axial Quantitative Uniformity Measurements of Total-body PET Systems. *J Nucl Med.*, 2021;62 (suppl 1):3041.
3. Leung EK, Berg E, Omidvari N, et al. Quantitative accuracy in total-body imaging using the uEXPLORER PET/CT scanner. *Phys Med Biol.*, 2021;66(20).

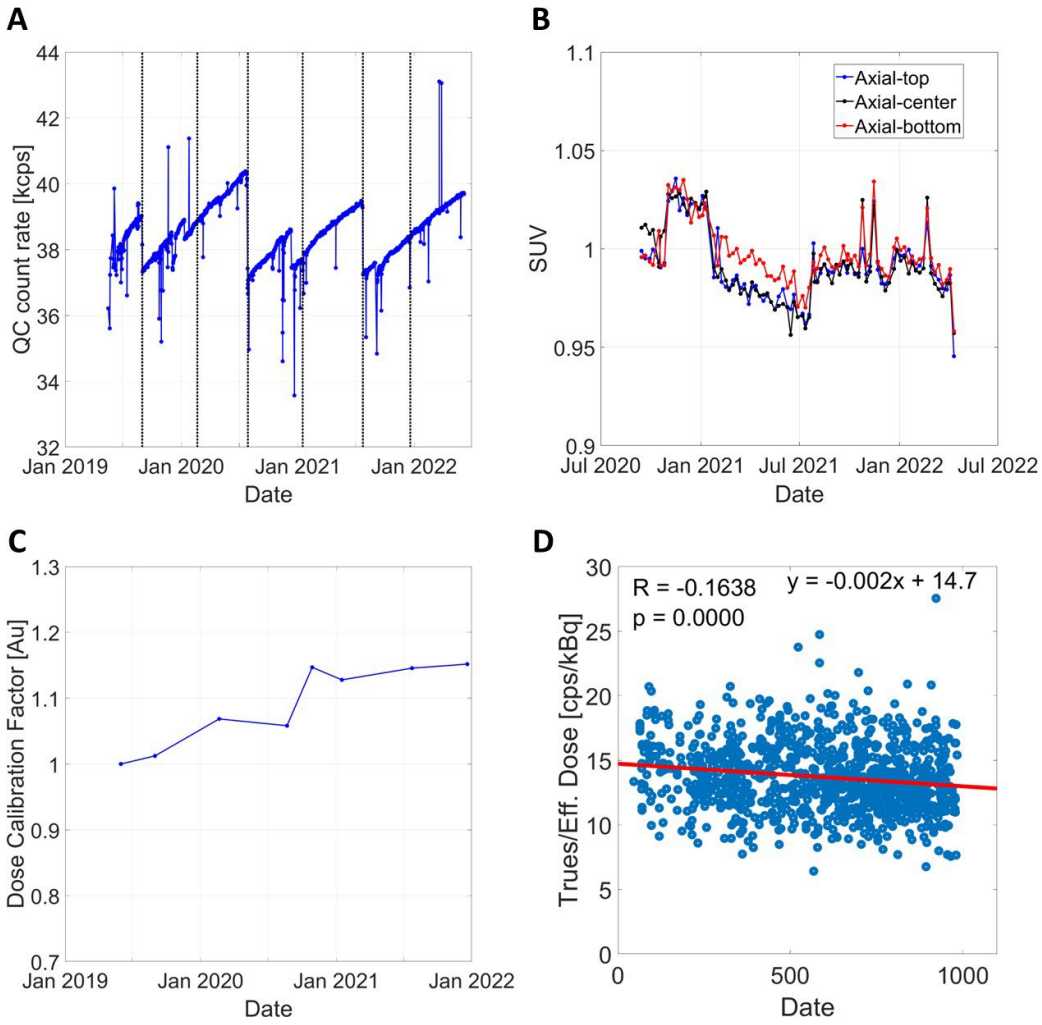

Figure 1. (**A**) Daily LYSO background count-rate measured over three years, where dotted vertical lines indicate dates of calibration. (**B**) Weekly ^{68}Ge uniform cylinder measurement over three years showing quantitative stability within 3% axially and within 5% over 2 years. (**C**) Dose calibration factor measured over three years. (**D**) Ratio of trues count-rate over the injected dose at scan time from 942 clinical ^{18}F-FDG exams during a 900-day period. The spread in the data is likely due to physiologic factors such as the size of the patient and the radioactivity amount voided by the patient.

Deep Multiclass Multiple Instance Learning for DSA Classification

Reza Moein Taghavi, B.A.
Roger Goldman, MD, Ph.D.

Introduction: Anatomic localization is essential for angiography interpretation. Many images in digital subtraction angiography (DSA) sequences lack sufficient localization due to limited contrast, posing challenges to automated interpretation. Our study evaluated a deep multiclass Multiple Instance Learning (MIL) algorithm for this purpose.

Methods: We reviewed the institutional PACS, identifying 689 DSA sequences performed with contrast administration via the aorta, left external iliac artery, right external iliac artery, celiac artery, superior mesenteric artery, and inferior mesenteric artery. Images were manually labeled as “key” if they showed contrast in the artery and a downstream vessel. The data comprised 482 sequences for training and validation and 207 for testing. Using MONAI Python library, we developed an MIL model.

The model was trained with inputs of 50 images from each angiographic sequence. We measured accuracy, precision, recall, and F1. The MIL model determined attention weights for each image's contribution to final classification. Images corresponding to the algorithmically generated top five attention weights were compared with manually-labeled “key” images for overlap. The overlap was quantified as the ratio of the number of images in common to the number of key images.

Results: The MIL algorithm achieved 92.75% accuracy (95% CI: 89.22 - 96.28), Precision: 93.99% ± 3.24, Recall: 92.75% ± 3.53, and F1: 88% ± 4.43 on the test data. Figure 1 depicts an example of a DSA image sequence. An average overlap of 54.8% was noted. In 93.24% of cases, at least one model-picked image matched a manually-labeled “key” image.

Discussion: The algorithm demonstrated robust performance. Given the high percent overlap, the future iterations of this algorithm can be used for labeling DSA data.

Conclusion: Deep learning with attention mechanisms can be harnessed for automatic classification of anatomical locations in DSA data, a crucial step for interpretation of images during and after endovascular procedures.

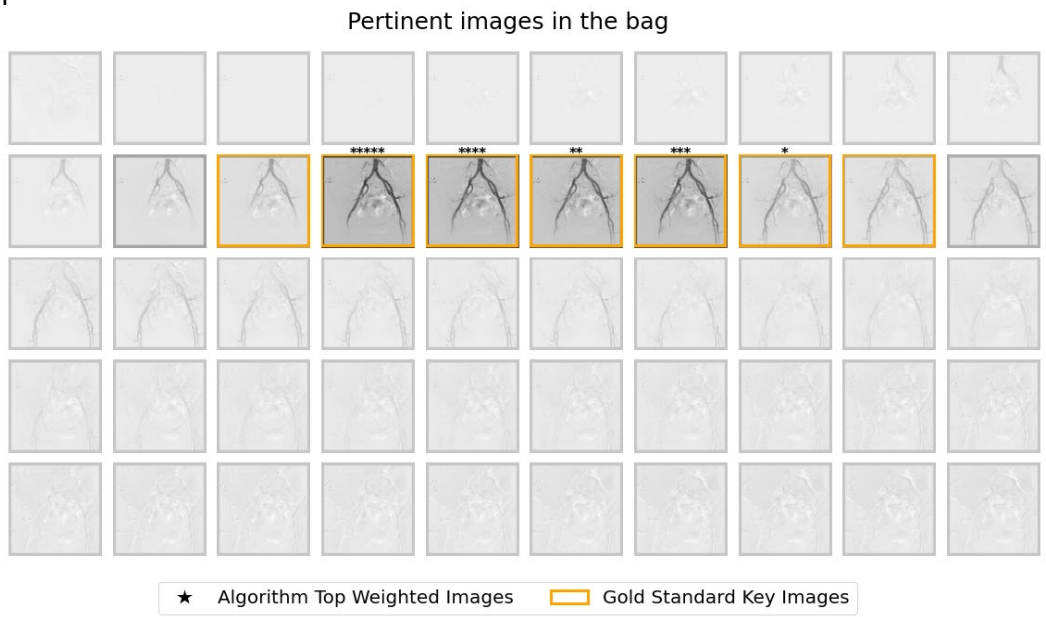

Figure 1: Sample DSA sequence from the testing dataset. Images with stars represent the top five weighted images by the algorithm, with the star count correlating to the assigned weight. Similarly, the opacity of the images correlates to algorithm generated weights: the greater the opacity, the larger the weight. Conversely, more transparent images have smaller weights. Images outlined in yellow rectangles represent the manually-labeled “key” images.

Total-body PET quantification of metabolism in non-alcoholic steatohepatitis using a three-tissue compartment model

Quyen Tran, Victoria Lyo, Karen E. Matsukuma, Michael T Corwin, Benjamin A. Spencer, Yiran Wang, Sean K. Romeo,
Valentina Medici, Simon R. Cherry, Ramsey D. Badawi, Souvik Sarkar, and Guobao Wang
University of California – Davis

Objective. Nonalcoholic steatohepatitis (NASH) is a metabolic disease that affects many patients worldwide. PET with ^{18}F-fluorodeoxyglucose (FDG) has the potential to characterize the disordered energy metabolism in NASH but has not been feasible to show this ability using standard static imaging or dynamic imaging with a standard temporal resolution (e.g., 10-20s/frame). Early work using dynamic FDG-PET showed measuring the change in glucose transport but not in glucose metabolism (Wang *et al, Phys. Med. Biol.* 63(2018) 155004). Herein, we demonstrate the use of high-temporal resolution (2s/frame) dynamic imaging and kinetic modeling enabled on total-body PET to characterize organ metabolism in healthy subjects and those with NASH.

Method. 14 healthy subjects and 25 patients with nonalcoholic fatty liver disease (NAFLD) were included in this study and scanned on an uEXPLORER total-body PET/CT system for one hour. Histologically-proven NASH was defined by NAFLD activity score (NAS) greater than 4. Regions of interest (ROI) were placed in the descending aorta to extract an image-derived blood input function, and in the liver, gray matter, and spleen to extract tissue time activity curves (TACs). Both the conventional two-tissue (2T) model, which combines the interstitial space and intracellular space into a free-state space, and the proposed three-tissue (3T) model, which separately models the interstitial space, were used to fit the high-temporal resolution TACs. Furthermore, the effect of dual blood supply was modeled with the 2T and 3T models for liver kinetic modeling. Standardized uptake value (SUV) at one hour postinjection and the net influx rate K_i estimated with the 2T and 3T models were used to characterize glucose metabolism and compared between the non-NASH group (29 subjects, including healthy subjects and NAFLD with a NAS $\leq$ 4) and NASH group (10 subjects) using statistical T-tests.

Result. The 3T model showed an improved TAC fitting in all organs as compared to the 2T model and had a lower Akaike information criterion value in all subjects (results not shown). The 3T K_i of the liver was higher in NASH than in non-NASH (P = 0.028) (Fig. A), which may reflect the increased energy metabolism of hepatic macrophages in NASH. Liver SUV (results not shown) and 2T K_i were not statistically different between the two groups (P > 0.16) (Fig. B). A metabolic difference was also observed in the spleen between NASH and non-NASH, but only by 3T K_i (P = 0.015) (Fig. C), not by SUV or 2T K_i (P > 0.52) (Fig. D). The increased metabolism in the spleen of patients with NASH can be partly explained by the fact that spleen is one of the major immune organs and its activity may be stimulated by distant inflammation. In the gray matter, SUV and 2T K_i did not differ significantly between NASH and non-NASH (P > 0.53) (Fig. F), but the improved fitting by the 3T model led to a significantly lower K_i in NASH (P = 0.005) (Fig. E). The result suggests a reduced energy metabolism in the brain of patients with NASH, in align with the hypothesis that neurodegeneration may occur in NAFLD and NASH (Mondal *et al, Journal of Neuroinflammation* 201(2020)).

Conclusion. Dynamic FDG-PET has the ability to characterize the changes of metabolism in NASH but it is only possible with a 3T compartmental model that accounts for the interstitial space, not by SUV or a conventional 2T model. The reported results suggest that NASH results in increased energy metabolism in the liver and spleen but decreased metabolism in the brain.

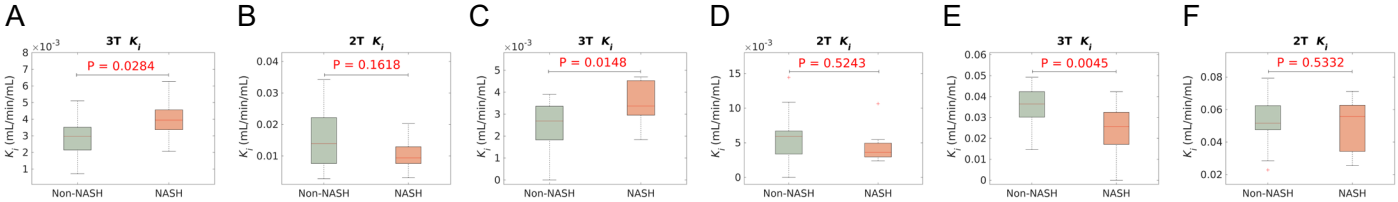

Liver: 3T K_i was higher in NASH than in non-NASH (A), while 2T K_i did not differ significantly (B). **Spleen:** 3T K_i was higher in NASH than in non-NASH (C), 2T K_i did not differ (D). **Gray matter:** 3T K_i was lower in NASH than in non-NASH (E), 2T K_i did not differ (F).

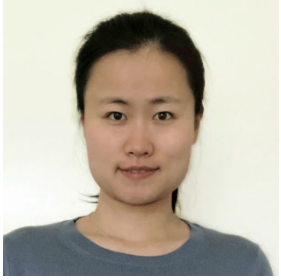

Spatial Resolution Estimation for UCD PET-MR Insert

Qian Wang, Aaron R Selfridge, Ramsey D Badawi, Felipe Godinez

Department of Biomedical Engineering, University of California, Davis
Department of Radiology, University of California, Davis

Introduction: A high-performance small-animal PET insert compatible with a commercial small-animal 7T MRI to enable simultaneous multimodal imaging is under development by our group. This study focused on exploring the spatial resolution that can be achieved by this PET insert.

Methods: The established PET insert system has 16 detector blocks in a ring and 4 block rings. Each block contains an array of 19×19 LYSO crystals with the dual-ended readout to yield the depth of interaction (DOI) information. The crystal has a cross-sectional area of 0.93×0.93 mm^2 with 1 mm pitch, and a thickness of 20 mm. This system therefore has a ring diameter of 102 mm and an axial field of view (FOV) of 79 mm considering the gaps between blocks. The list-mode OSEM algorithm with DOI information integrated was used to reconstruct images. A 5-cm-diameter ^{68}Ge cylinder placed at the center of the FOV was scanned for 25 hours for normalization. The direction normalization, attenuation, delay-window-based random and single-scatter-simulation-based scatter corrections were included in the image reconstruction. The reconstructed images have fine voxels with the voxel sizes of 0.56×0.56 (transaxial) ×0.5 (axial) mm^3 and 0.28×0.28 (transaxial) ×0.25 (axial) mm^3. A micro-Derenzo phantom with rod diameters of 4.8, 4.0, 3.2, 2.0, 1.6, and 1.2 mm was scanned for 1 hour. A ^{22}Na point source placed accordingly to the NEMA NU-4 protocol was imaged to estimate the spatial resolution, in terms of the FWHMs of the point peak along radial, tangential and axial directions.

Results: The micro-Derenzo images were reconstructed using two voxel sizes and the smallest rods with the diameter of 1.2 mm are differentiable. The spatial resolution of the PET insert at the FOV center is 1.3 1.4 and 1.6 mm in radial, tangential and axial directions, respectively.

Conclusion and Discussion: The spatial resolution of the PET insert was estimated. The point spread function modeling will be added, and the point source will be added a background to avoid spatial resolution overestimation.

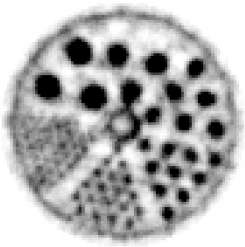

	Radial	Tangential	Axial
FWHM (mm)	1.34	1.40	1.56
FWTM (mm)	3.46	3.75	4.70

Figure. Mini-Derenzo image using voxel size of 0.56×0.56×0.5 mm^3. Normalization but no other corrections were applied.

Table. Spatial resolution, in terms of the FWHM and FWTM over the peak of a point source at the FOV center.

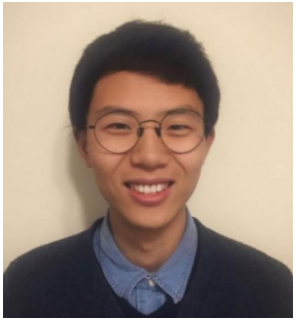

Impact of Dual-Blood Input Function on Kinetic Modeling of Lung Tumors Using Total-Body PET

Yiran Wang, Yasser G Abdelhafez, Benjamin A Spencer, Rashmi Verma, Mamta Parikh, Nicholas Stollenwerk, Lorenzo Nardo, Terry Jones, Ramsey D Badawi, Simon R Cherry, Guobao Wang

INTRODUCTION: The lungs are supplied by two blood vessels: the pulmonary artery, which originates from the right ventricle (RV), and the bronchial arteries, which are downstream from the left ventricle (LV). The blood supply of normal lung tissue is usually dominated by the pulmonary artery, while lung tumors can have an increased supply from the LV. However, this dual-blood supply has never been observed using PET. In this study, we proposed the dual-blood input function (DBIF) to model the dual-blood supply of the lung using high-temporal resolution (HTR) dynamic imaging on the uEXPLORER total-body PET.

METHODS: Thirteen healthy subjects and seven patients with three primary lung tumors and six lung metastases had a dynamic ^{18}F-FDG scan on the uEXPLORER. The reconstructed HTR dynamic images had 1s frames in the early phase. The extracted time activity curves (TACs) of normal lung and the tumors were fitted with compartment model using different input functions: the right ventricle input function (RVIF) $C_p^{RVIF}(t)=C_{RV}(t)$, the left ventricle input function (LVIF) $C_p^{LVIF}(t)=C_{LV}(t)$, and the dual-blood input function (DBIF) $C_p^{DBIF}(t)=fC_{LV}(t)+(1-f)C_{RV}(t)$ with f denoting the LV supply fraction. TAC fitting of the models was examined, and the f was compared between the normal lung and tumors. Multiparametric images by the DBIF model were generated.

RESULTS: The two peaks in the tumor TAC correlated with its dual-blood supply and was fitted best by the DBIF model (Fig. 1A). The parameter f was low in normal lung (0.037±0.013) but higher in tumors (0.30±0.25) with $P<0.0002$ (Fig. 1B). Multiparametric images by DBIF showed distinct tracer kinetics between normal tissue and tumors (Fig. 1C).

CONCLUSION: The dual-blood supply in the lung was demonstrated using HTR dynamic imaging on total-body PET and the DBIF model. The DBIF modeling improved lung kinetic quantification to differentiate lung tumors from normal lung tissue.

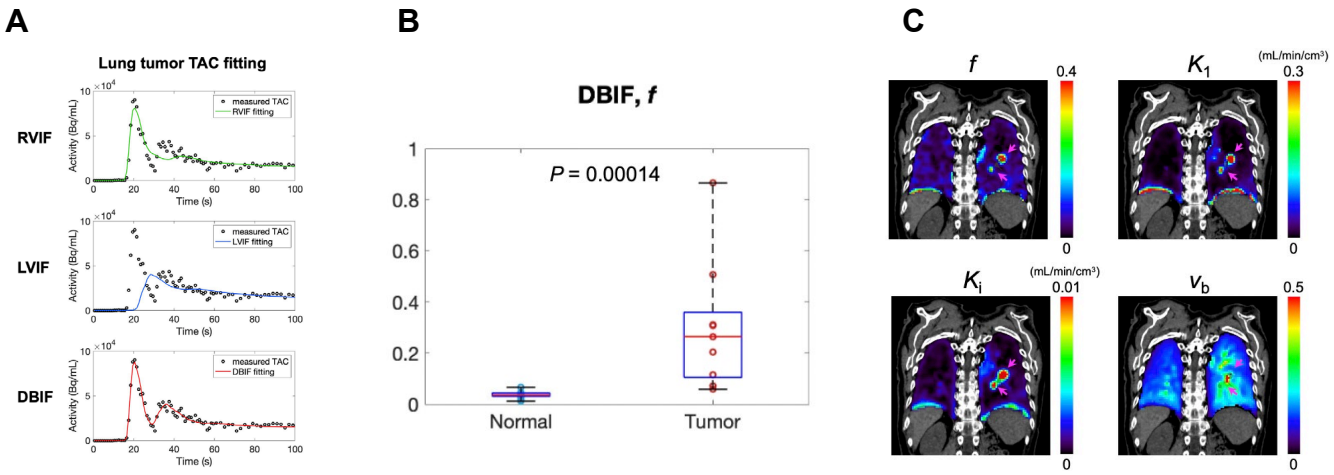

Figure 1. A. The measured TAC of a lung tumor and TAC fittings with the models of RVIF, LVIF, and the proposed DBIF. B. the LV contribution f estimated by the DBIF model in the two groups. C. Multiparametric images of the segmented lung of a subject with lung tumors: LV supply contribution f, ^{18}F-FDG delivery rate K_1, ^{18}F-FDG net influx rate K_i, and fractional blood volume v_b generated with the proposed DBIF model. The arrows point to lung tumors.

A Dosimetric Comparison of Y-90 Radioembolization, Stereotactic Body Radiation Therapy and HDR Brachytherapy for Treatment of Liver Cancer

Kajetan Wysoczynski, Brahim Mehadji, Peter Park, Jon Hunt, Stanley Benedict, Emilie Roncali University of California, Davis, CA, USA

Introduction: Liver cancer treatment is a high-impact clinical area with rising mortality. More insight is required to choose between modalities. This study compares dose distribution and conformity of several treatment planning methods, including Y-90 microsphere radioembolization, stereotactic body radiation therapy (SBRT), and HDR brachytherapy.

Methods: Five patients with hepatocellular carcinoma underwent Y-90 treatment, then a positron emission tomography (PET) / CT scan. Radioembolization dosimetry was based on the PET scan and contours delineated on CT images. The same contours were used to simulate four-fraction plans using a conventional SBRT linac with 5 mm leaf width. Single-fraction HDR brachytherapy plans were simulated with a maximum of 5 catheters. Dose distributions of the three modalities were compared for several organs based on dose-volume histograms.

Results: Y-90 radioembolization allows for delivery of the highest local dose - 82% of a large (227 mL) tumor volume received 100 Gy, where SBRT had a 75 Gy maximum. Brachytherapy allows for high conformity in smaller tumors; in one patient, at least 99% of the tumor volume received 34 Gy, but there was a hotspot of 199 Gy at 3% volume.

Discussion: Dose should be maximized for the target and minimized for healthy tissue. Brachytherapy allows for high dose delivery in small tumors. However, it is suboptimal for large tumors as many needles would be required. SBRT delivers the most homogeneous dose distribution to the tumor, with a maximum rarely exceeding 125% of prescription. Y-90 data showed localized doses of up to 900 Gy to the tumor, but careful planning and well-vascularized tumors are needed for successful treatment.

Conclusion: All three studied modalities are viable for liver cancer treatment. Brachytherapy can offer excellent conformity at the cost of invasive administration. In future studies, biologically effective dose will be considered instead of physical dose and proton therapy will be included.

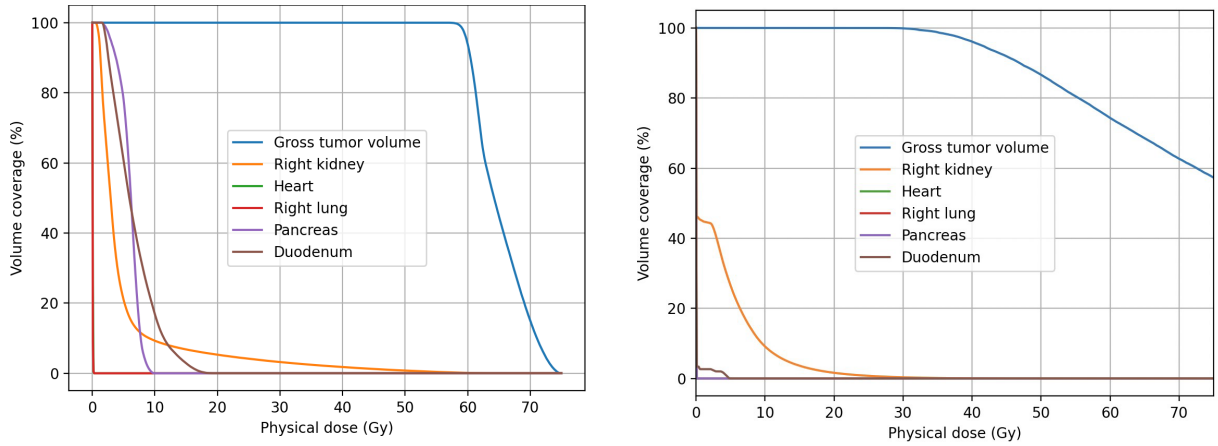

Figure 1: A patient with a small tumor (7.7 mL volume). The left graph shows a dose-volume histogram for SBRT, while the right graph shows HDR brachytherapy data. SBRT exhibits a more homogeneous dose distribution and reaches the prescribed 60 Gy at 93.9% volume, while HDR reaches prescribed 30 Gy at 100% volume. Both modalities spared surrounding organs as defined by regulations, but brachytherapy offered a lower dose compared to SBRT.

Generalized Calibrated BOLD fMRI for the Relationship between Cerebral Metabolism and Hypertensive Status

Anqi Zhang[1], Donghoon Kim[1], Sarah Y Hong[1], Timothy M. Hughes[2], Samuel N. Lockhart[2], Suzanne Craft[2], Laura D. Baker[2], Christopher T. Whitlow[2], Stephanie E. Okonmah-Obazee[2], Christina E. Hugenschmidt[2], Matthew Bobinski[1], Youngkyoo Jung[1]

1. University of California, Davis, California
2. Wake Forest School of Medicine, Winston-Salem, North Carolina

Introduction: Hypertensive status during mid-life have been found to be associated with an increased susceptibility to developing dementia later in life. Quantitative imaging biomarkers, such as Oxygen Extraction Fraction (OEF) and Cerebral Metabolism Rate of Oxygen (CMRO2), can be indicators of impaired cerebral metabolism. Calibrated Blood Oxygen Level Dependent (BOLD) functional Magnetic Resonance Imaging (fMRI) is a multi-parametric approach utilizing hyperoxic and hypercapnic gas challenges. The impact of hypertension on OEF and CMRO2 has been investigated.

Method: A cohort of 84 participants was recruited from the Wake Forest Alzheimer's Disease Research Center (ADRC) Clinical Core. Prediabetic and diabetic participants were considered diabetic. Participants with hypertension or on medication were classified as hypertensive. The MRI was conducted using a 3T Siemens Skyra MRI scanner with a 32-channel head coil. Dynamic Pseudocontinuous Arterial Spin Labeling (PCASL) was used to acquire cerebral blood flow (CBF) and BOLD images during respiratory challenges with an end-tidal forcing system. The ROI values in the frontal lobe, temporal lobe, parietal lobe, and occipital lobe regions were chosen. The correlation between hypertension and OEF and CMRO2 in the ROI was analyzed with a linear mixed model, with covariates of age, sex, cognitive status, APOE genotype, diabetic status, and hypertensive status.

Results: A negative correlation was found between CBF, OEF, and CMRO2 with hypertensive status in frontal lobe region (Figure 1). Statistical significance was observed for OEF and CMRO2 ($p = 0.049$ and $p = 0.028$, respectively), indicating the potential influence of hypertensive status on these biomarkers.

Conclusion: The study concludes that there is a significant negative association between hypertensive status and both OEF and CMRO2 in the frontal lobe region. The observed reduction in OEF and CMRO2 is not solely due to decreased CBF, but rather complex and multifactorial processes involving vascular remodeling and altered oxygen metabolism.

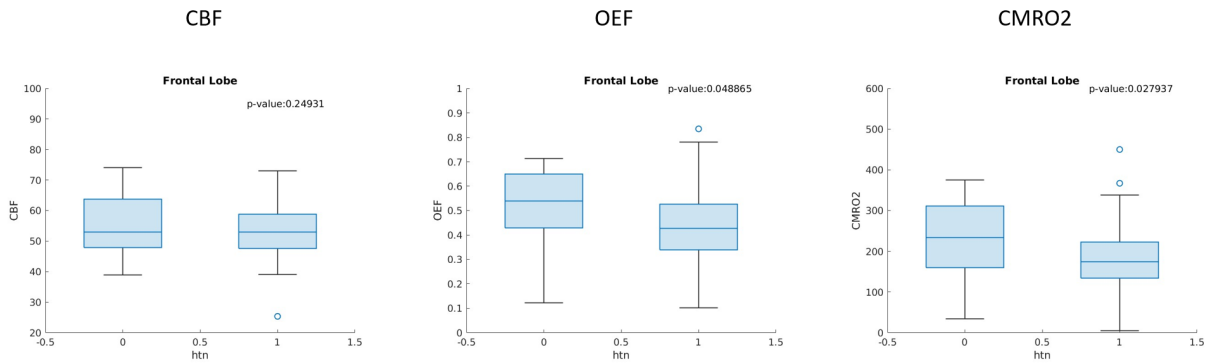

Figure 1. Boxplots representing the contribution of hypertensive status to reduced CBF, OEF, and CMRO2 values in the frontal lobe

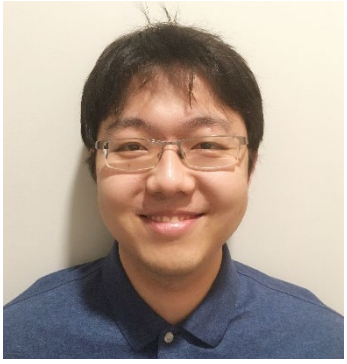

Super-resolution reconstruction of gamma-ray CT images for PET-enabled dual-energy CT imaging

Yansong Zhu[1], Benjamin A. Spencer[1,2], Zhaoheng Xie[2], Edwin K. Leung[3], Reimund Bayerlein[1], Negar Omidvari[2], Simon R. Cherry[2,1], Jinyi Qi[2], Ramsey D. Badawi[1,2], Guobao Wang[1]

[1]Department of Radiology, University of California, Davis

[2]Department of Biomedical Engineering, University of California, Davis

[3]UIH America, Inc., Houston, Texas

Introduction: PET-enabled dual-energy CT (PDECT) generates PET and DECT images simultaneously with a conventional PET/CT scanner without the need for a second x-ray CT scan. It provides additional tissue-fraction information for PET/CT imaging and could potentially improve the characterization of diseases. In PDECT, gamma-ray CT (gCT) images at 511 keV are obtained from time-of-flight (TOF) PET data and are combined with the existing x-ray CT images to form DECT images. We have developed a kernel-based maximum-likelihood attenuation and activity (kMLAA) method that uses x-ray CT images as *a priori* information for noise suppression. Previously, we focused on gCT image reconstruction at the PET image resolution which is coarser than standard CT image resolution. Here we explored the feasibility of generating super-resolution gCT images at the corresponding CT resolution.

Methods: The existing kMLAA utilizes x-ray CT image at the PET resolution to build the kernel matrix. To generate super-resolution gCT images, kernel matrix is built directly from the x-ray CT image at the CT resolution. Both phantom and patient scans were used to evaluate the method. gCT images at the PET resolution with a pixel size of 4.0 mm × 4.0 mm and at the CT resolution with a pixel size of 1.2 mm × 1.2 mm were reconstructed using both the standard MLAA and kMLAA methods.

Results: The gCT images at the CT resolution showed sharper edges more structural details compared to the images reconstructed at the PET resolution. Images from the kMLAA method showed substantially improved image quality compared to those obtained with the standard MLAA method.

Conclusion: We explored the feasibility of reconstructing super-resolution gCT images from TOF PET data at the CT image resolution. Results showed that super-resolution gCT images from kMLAA have improved image quality and reveal more details compared to gCT images at PET resolution.

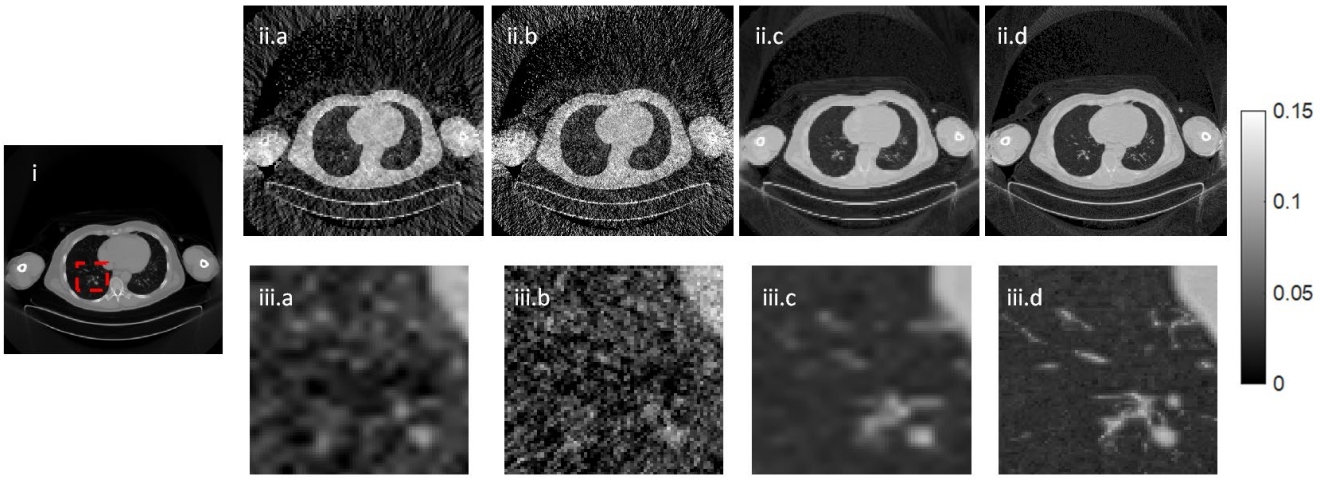

Fig. 1: Results of patient data for (i) 80 kVp x-ray CT image, the red box indicates the region for zoomed-in views, (ii) gCT images and (iii) zoomed-in views of the gCT images reconstructed with (a) MLAA at the PET resolution, (b) MLAA at the CT resolution, (c) kMLAA at the PET resolution, and (d) kMLAA at the CT resolution.